

# Wetting transition of ionic liquids at metal surfaces: A computational approach to electronic screening using a virtual Thomas-Fermi fluid

Alexander Schlaich,<sup>1,\*</sup> Dongliang Jin,<sup>1</sup> Lyderic Bocquet,<sup>2</sup> and Benoit Coasne<sup>1,†</sup>

<sup>1</sup> Univ. Grenoble Alpes, CNRS, LIPhy, 38000 Grenoble, France

<sup>2</sup> Laboratoire de Physique de l'Ecole Normale Supérieure, CNRS, Université PSL, Sorbonne Université, Sorbonne Paris Cité, Paris, France

We explore the behavior of charged systems, such as electrolytes and salts, in the vicinity of metallic confining surfaces — a situation relevant to many applications in energy, electrochemistry, etc. While existing molecular simulation strategies consider perfect metal or insulator surfaces, we develop here an effective approach that allows dealing with any real metal between these asymptotes. Building on the Thomas–Fermi (TF) formalism for electronic screening, electrostatic interactions in the metal are described through the behavior of a ‘virtual’ Thomas-Fermi fluid of charged particles, whose Debye length sets the TF screening length  $\lambda$  in the metal. This easy-to-implement molecular method captures the electrostatic interaction decay upon varying  $\lambda$  from insulator to perfect metal conditions. By applying this strategy to a nanoconfined ionic liquid, an unprecedented wetting transition is found upon switching the confining medium from insulating to metallic.

The fluid/solid interface as encountered in confined liquids is the *locus* of a broad spectrum of microscopic phenomena such as molecular adsorption, chemical reaction, and interfacial slippage [1]. These molecular mechanisms are key to nanotechnologies where the fluid/solid interaction specificities are harnessed for energy storage, catalysis, lubrication, depollution, etc. From a fundamental viewpoint, the behavior of nanoconfined fluids often challenges existing frameworks even when simple liquids are considered. Ionic systems, either in their liquid or solid state, between charged or neutral surfaces lead to additional ion adsorption, crowding/overscreening, surface transition, and chemical phenomena that are crucial in electrokinetics (e.g. electrowetting) and electrochemistry (e.g. supercapacitors/batteries) [2]. Theoretical descriptions of nanoconfined fluids — except rare contributions [3–7] — assume either perfectly metallic or insulating confining surfaces but these asymptotic limits do not fully reflect real materials as they display an intermediate imperfect metal/insulator behavior (only few metals behave perfectly and all insulators are semi-conducting to some extent). Yet, the electrostatic boundary condition imposed by the surrounding medium strongly impacts confined dipolar and, even more, charged systems [8–10]. For instance, confinement-induced shift in the freezing of an ionic liquid was found to drastically depend on the surface metallic/insulating nature [11].

Formally, the electronic screening occurring in the confining metallic walls can be accounted for using the microscopic Thomas–Fermi (TF) model [11, 12]. This semi-classical formalism allows considering any real metal — from perfect metal to insulator — through the Thomas–Fermi screening length  $\lambda$ . The latter is defined in terms of the electronic density of state of the metal at the Fermi level  $\mathcal{D}(\mathcal{E}_F)$  according to  $\lambda = \varepsilon/e^2\mathcal{D}(\mathcal{E}_F)$  ( $\varepsilon$  is the dielectric constant and  $e$  the elementary charge); the Fermi energy is directly related to the free electron density  $n_0$  as  $\mathcal{E}_F = \hbar^2(3\pi^2n_0)^{2/3}/(2m_e)$  where  $m_e$  is the elec-

tron mass and  $\hbar = h/2\pi$  the Planck constant, see *Supplemental Material*. Despite this available framework, the development of classical molecular simulation methods to understand the microscopic behavior of classical fluids in contact with imperfect metals is only nascent. While insulators are treated using solid atoms with constant charge, metals must be described using an effective screening approach. The charge image concept can be used for perfectly metallic and planar surfaces (e.g. Ref. [13]) but refined strategies must be implemented for non-planar surfaces such as a variational [14, 15] or Gauss law [16–18] approaches to model the induced charge distribution in the metal. A recent proposal [4] builds on our TF framework [3] to propose a computational approach based on variational localized surface charges that accounts for electrostatic interactions close to imperfect metals.

Here, we develop an effective yet robust atom-scale simulation approach which allows considering the confinement of dipolar or charged fluids between metallic surfaces of any geometry and any TF electronic screening length. Following Torrie and Valleau’s work for electrolyte interfaces [19], the electronic screening in the imperfect confining metal is accounted for through the response of a high temperature virtual Thomas–Fermi fluid made up of light charged particles. Due to its very fast response, this effective TF fluid mimics metal induction within the confining surfaces upon sampling the confined system configurations using Monte Carlo or molecular dynamics simulations. After straightforward implementation in existing simulation packages, this strategy provides a mean to impose an effective electronic TF screening length that is directly linked to the equivalent virtual fluid Debye length. This model correctly captures electrostatic screening within the confined system upon varying the confining host from perfect metal to insulator conditions. Using this novel method, by considering an ionic liquid between two parallel planes, we unravel a

continuous wetting transition as the surfaces are tuned from insulating (non-wetting) to metallic (wetting).

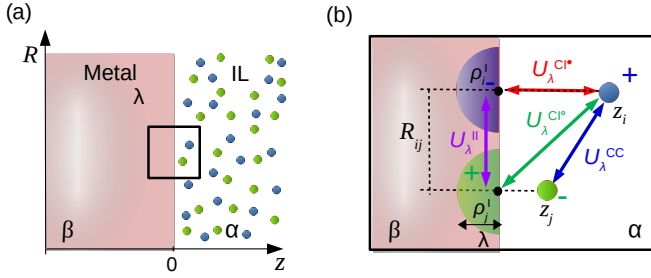


FIG. 1. (a) Ionic liquid (IL) in an insulating medium  $\alpha$  close to an imperfect metal  $\beta$  having a Thomas–Fermi length  $\lambda$ . (b) One and two-body interactions for two point charges  $i, j$  at distances  $z_i$  and  $z_j$  from the surface and separated by in-plane distance  $R_{ij}$ . The induced charge distribution  $\rho_k^I(\mathbf{r})$  for  $k = i, j$  (denoted by half-ellipsoids) within the metal is of opposite sign and decays over  $\lambda$ . The colored arrows show the different energy contributions given in Eq. (1).

*Interaction at Thomas–Fermi metal interfaces* — Fig. 1(a) depicts point charges in an insulating medium  $\alpha$  of relative dielectric constant  $\varepsilon_\alpha$  close to a metal  $\beta$  of TF length  $\lambda$ . As shown in the *Supplemental Material*, the electrostatic energy of two charges  $i$  and  $j$  at distances  $z_i$  and  $z_j$  from the dielectric/metal interface and separated by  $r_{ij} = [R_{ij}^2 + (z_i - z_j)^2]^{1/2}$  with  $R_{ij}$  the in-plane distance reads:

$$U_\lambda(z_i, z_j, R_{ij}) = U_{\lambda}^{\text{CC}}(r_{ij}) + U_{\lambda}^{\text{CI}}(z_i, z_j, R_{ij}) + U_{\lambda}^{\text{II}}(z_i, z_j, R_{ij}). \quad (1)$$

where the superscripts C and I refer to the physical charges in the dielectric medium and induced charges within the metal, respectively. As shown in Fig. 1(b),  $U_{\lambda}^{\text{CC}}$  is the Coulomb interaction energy between the charges  $i$  and  $j$  while  $U_{\lambda}^{\text{II}}$  is the interaction energy between the charge densities  $\rho_i^I$  and  $\rho_j^I$  induced in the metal by these two charges. For each ion  $i$ , its interaction energy  $U_{\lambda}^{\text{CI}}$  with the metal decomposes into a one-body contribution  $U_{\lambda}^{\text{CI}*}(z_i)$  — corresponding to the interaction with its image in the metal — and two-body contributions  $U_{\lambda}^{\text{CI}^o}(z_i, z_j, R_{ij})$  — corresponding to the interaction with the induced charges due to all other charges  $j$ . Analytical expressions exist for  $U_{\lambda}^{\text{CI}*}$  and  $U_{\lambda}^{\text{CI}^o}$  [3, 5] but  $U_{\lambda}^{\text{II}}$  must be estimated numerically from the energy density, i.e.  $U_{\lambda}^{\text{II}} = \int d\mathbf{r} \Psi_i^\beta(\mathbf{r}) \rho_j^I(\mathbf{r}) + \Psi_j^\beta(\mathbf{r}) \rho_i^I(\mathbf{r})$ , where  $\Psi_k^\beta$  and  $\rho_k^I$  are the electrostatic potential and induced charge density in the metal due to the point charge  $k = i, j$ . All details are given in the *Supplemental Material*.

*Effective molecular simulation approach* — Except for the usual Coulomb energy CC, formal expressions for the CI and II energies cannot be implemented in molecular simulation due to their complexity. In particular,

$U_{\lambda}^{\text{II}}$  requires expensive integration on the fly as analytical treatment for imperfect metals is only available in closed forms in asymptotic limits [3, 7]. Here we model the resulting complex electrostatic interactions between the ions of the liquid thanks to a ‘virtual Thomas–Fermi fluid’ located within the confining solids, see Fig. 2(a). Our approach builds on the direct analogy between the Thomas–Fermi screening of electrons and the Debye–Hückel equation for electrolyte solutions. In the linear Thomas–Fermi formalism, the induced electronic charge density in the metal writes:  $q_{\text{TF}} \rho^I(\mathbf{r}) = -\varepsilon_0 \varepsilon_\beta k_{\text{TF}}^2 \Psi_\beta(\mathbf{r})$  where  $\varepsilon_0$  is the vacuum permittivity,  $\varepsilon_\beta$  the relative dielectric constant,  $k_{\text{TF}} = [e^2 \mathcal{D}(\mathcal{E}_F) / \varepsilon_0 \varepsilon_\beta]^{1/2}$  the Thomas–Fermi wave-vector, and  $\mathcal{D}(\mathcal{E}_F)$  the density of states at the Fermi level (see *Supplemental Material*). Combined with Poisson equation this leads to the Helmholtz equation for TF screening,  $\nabla^2 \Psi_{\text{II}} = k_{\text{TF}}^2 \Psi_{\text{II}}$ , which indeed resembles the Debye–Hückel equation for electrolyte solutions. Accordingly, one can simulate the imperfect metal using a system of virtual (classical) charged particles of charge  $q_{\text{TF}}$  and mass  $m_{\text{TF}}$ , with density  $\rho_{\text{TF}}$  and temperature  $T_{\text{TF}}$ . The analogous TF screening length  $\lambda = k_{\text{TF}}^{-1}$  can be identified as the equivalent Debye length  $\lambda_D$ :

$$\lambda \sim \lambda_D = \sqrt{\frac{\varepsilon_\beta \varepsilon_0 k_B T_{\text{TF}}}{\rho_{\text{TF}} q_{\text{TF}}^2}}. \quad (2)$$

Hence, by considering the dynamics of these light ions located in the confining solid, any screening length  $\lambda$  between 0 (perfect metal) and  $\infty$  (insulator) can be efficiently mimicked depending on  $q_{\text{TF}}$ ,  $\rho_{\text{TF}}$ , and  $T_{\text{TF}}$ . This virtual system allows simulating properly the complex electrostatic interactions within the ionic liquid in the vicinity of an imperfect metal.

Eq. (2) shows that mapping the fluid of mobile charges onto the TF model only requires to set  $\rho_{\text{TF}} q_{\text{TF}}^2 / T_{\text{TF}}$  (fixing  $\varepsilon_\beta = 1$ ). In our molecular dynamics approach, to ensure that the particles in this effective Thomas–Fermi fluid relax fast, their mass/temperature are chosen much smaller/larger than their counterpart in the confined system; typically  $m_{\text{TF}} \sim 0.01m$  and  $T_{\text{TF}} \sim 10T$  (requiring typical integration steps of 0.1 fs and 1 fs, respectively). In practice, as shown in Fig. 2(a), the effective simulation strategy consists of sandwiching the charged or dipolar system between two metallic media separated by  $d_w = 20\text{ nm}$ . The confining media with length  $d_{\text{TF}} = 10\text{ nm}$  are filled with the Thomas–Fermi fluid having a density  $\rho_{\text{TF}} = 57.5\text{ nm}^{-3}$ . Periodic boundary conditions are used in all dimensions and reflective walls are used at each metal/dielectric interface to prevent the Thomas–Fermi fluid/charged system to migrate to the pore space/confining media. Once  $\rho_{\text{TF}}$  and  $T_{\text{TF}}$  are set,  $\lambda$  is varied by tuning  $q_{\text{TF}}$  according to Eq. (2); from  $q_{\text{TF}} = 0$  ( $\lambda \rightarrow \infty$ ) for an insulator to  $q_{\text{TF}} = 1$  ( $\lambda = 0.03\text{ nm}$ ) for a nearly perfect metal. All simulations are carried out using LAMMPS [20] with electrostatic in-

teractions calculated using the PPPM method. To prevent opposite charge overlap in the Thomas–Fermi fluid, a power-law repulsion  $\sim 1/r^n$  is used but we checked that our results are independent of the detailed interaction (details are provided in the *Supplemental Material*).

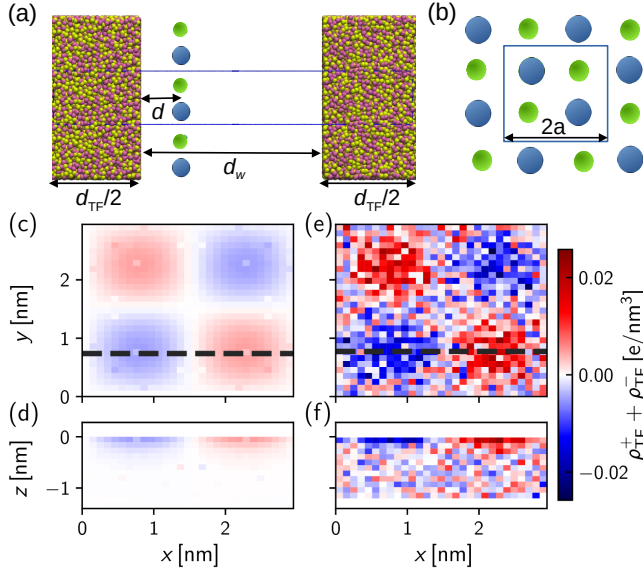


FIG. 2. (a) 2D ionic crystal (blue/green charges) at a distance  $d = 0.22$  nm from a medium in which electrostatic screening is modeled using a Thomas–Fermi fluid (yellow/pink charges). The crystal layer is confined in a pore of width  $d_w$  while the Thomas–Fermi fluid occupies a region width  $d_{TF}$ . (b) Top view of the 2D ionic crystal (lattice constant  $a$ ) illustrating the periodic boundary conditions. (c)-(d) Top/side views of the induced charge density  $\rho^I(d, \mathbf{r})$  in a Thomas–Fermi fluid as obtained from Eq. (3) for the system in (a). (e)-(f) Same as (c)-(d) but using our simulation approach. The screening length as defined in Eq. (2) is  $\lambda = 0.25$  nm.

*2D crystal at metallic interfaces* — To validate our effective approach, we consider a 2D square crystal of lattice constant  $a = 1.475$  nm made up of charges  $\pm 1$  e and located at a distance  $d$  from a metal (Fig. 2). Due to the periodic boundary conditions, a second pore/metal interface is present at a distance  $d_w = 20$  nm. Yet, as shown in the *Supplemental Material*, this second interface does not affect the electrostatic energy as  $d_w$  is large enough. In the Thomas–Fermi framework, the charge density  $\rho^I$  at a position  $\mathbf{r}$  in the metal induced by a charge  $q$  located in  $(0, 0, d)$  reads (see *Supplemental Material*):

$$\rho^I(d, z, R) = - \int_0^\infty dK K J_0(KR) \frac{\varepsilon_\beta k_{TF}^2 q e^{-Kd}}{2\pi (\varepsilon_\alpha K + \varepsilon_\beta \kappa)} e^{\kappa z}, \quad (3)$$

where  $R = [x^2 + y^2]^{1/2}$  is the lateral distance to the charge  $q$ ,  $J_0$  is Bessel function of the first kind, and  $\kappa^2 = K^2 + k_{TF}^2$ . Fig. 2(c,d) shows the induced charge density  $\rho^I(d, \mathbf{r})$  as obtained by summing Eq. (3) for the

2D crystal when  $d = 0.22$  nm and  $\lambda = k_{TF}^{-1} = 0.25$  nm (as discussed in the *Supplemental Material*, Eq. (3) must be summed over all crystal periodic images but it was found that the sum converges quickly). For comparison, Fig. 2(e,f) shows  $\rho^I(d, \mathbf{r})$  as obtained using our effective approach from the local charge density in the metal, i.e.  $\rho^I = e(\rho_{TF}^+ - \rho_{TF}^-)$ . In contrast to  $\rho^I(d, \mathbf{r})$  in the Thomas–Fermi model, due to their finite size, the fluid charges in the simulation cannot approach arbitrarily close to the metal/pore surface. For consistency, the analytical/simulation data were compared by defining  $z = 0$  in the simulation as the position where the Thomas–Fermi fluid density becomes non-zero. Fig. 2 shows that the effective molecular simulation qualitatively captures the predicted density distribution induced in the metal. Each physical charge in the 2D crystal induces in the metal a diffuse charge distribution of opposite sign. Moreover, as expected from the Thomas–Fermi framework, the induced charge distribution in the effective simulation decays over the typical length  $\lambda$ .

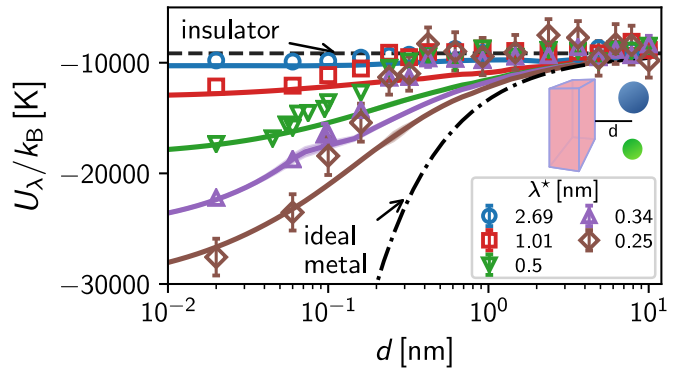


FIG. 3. Electrostatic energy  $U_\lambda(d)$  between a 2D ionic crystal and a Thomas–Fermi metal separated by a distance  $d$  for different  $\lambda$ . For each  $\lambda$ , the symbols correspond to the effective simulation while the solid line shows the linear Thomas–Fermi predictions.

Our effective approach was assessed quantitatively by probing the energy of the 2D ionic crystal as a function of its distance  $d$  to the metal surface for different screening lengths  $\lambda$ . The simulated electrostatic energy  $U_\lambda(d)$  consists of all ion pair contributions in Eq. (1) as discussed in the *Supplemental Material*. Figure 3 compares the total energy  $U_\lambda$  as a function of the distance  $d$  with the numerically evaluated prediction of the Thomas–Fermi model in Eq. (1). As expected theoretically, the overall energy decays with decreasing  $\lambda$  between boundaries for an insulator ( $\lambda \rightarrow \infty$ ) and a perfect metal ( $\lambda \rightarrow 0$ ). As shown in Fig. 3, our effective approach captures quantitatively the screening behavior of the confining medium assuming a screening length  $\lambda^* = c_0 + c_1 \lambda + c_2 \lambda^2$  ( $\lambda$  is the ion gas Debye length,  $c_0 = 0.23$  nm,  $c_1 = 0.64$  and  $c_2 = 1.78$  nm $^{-1}$  in our system). Such parameters, which

were fitted to match the simulated and theoretical energies at small  $d$ , account for the following effects in the screening fluid used in the simulation:  $c_0$  accounts for the finite size  $\sigma$  of the Thomas–Fermi ions which prevents reaching screening  $\lambda \leq \sigma$  (in line with the fact that  $c_0 \sim \sigma$ );  $c_1 \lesssim 1$  arises from the non-ideal behavior of the effective Thomas–Fermi fluid which screens less efficiently than an ideal gas having the same density  $\rho_{\text{TF}}$  ( $c_1 = 1$  corresponds to the ideal behavior);  $c_2 \neq 0$  indicates non-linear effects in electrostatic screening which go beyond the linear approximation used in the Thomas–Fermi framework.

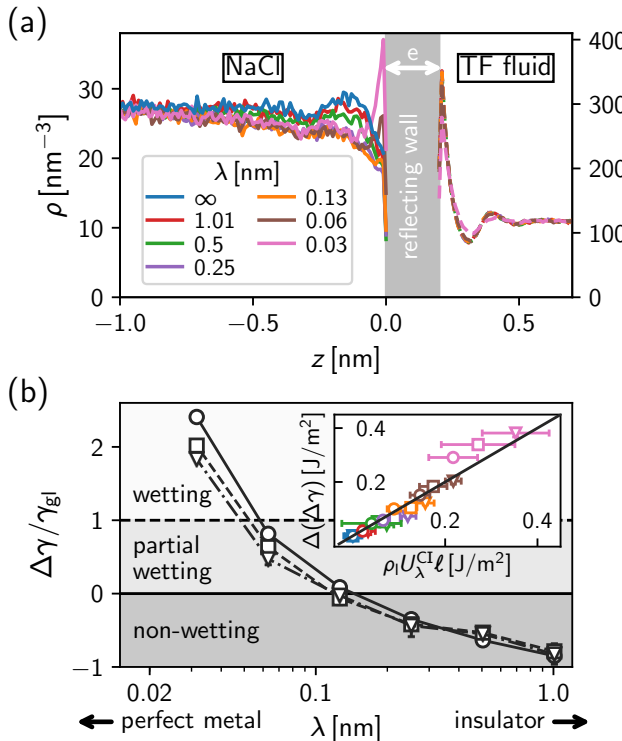


FIG. 4. (a) Density profile for a molten salt confined between metal surfaces with different screening lengths  $\lambda$ . The Thomas–Fermi fluid within the metal (right) and the molten salt (left) are separated by a reflective wall of thickness  $e = 0.2$  nm. The average salt density is  $\rho_l = 27$  nm<sup>-3</sup>. (b) Surface tension difference  $\Delta\gamma = \gamma_{\text{gm}} - \gamma_{\text{lm}}$  normalized by the gas/liquid surface tension  $\gamma_{\text{gl}}$  as a function of  $\lambda$ . Symbols indicate different liquid densities  $\rho_l$ : 27 nm<sup>-3</sup> (circles), 25 nm<sup>-3</sup> (squares) and 23 nm<sup>-3</sup> (triangles). The inset shows the change in the surface tension difference  $\Delta(\Delta\gamma(\lambda))$  between an insulator and the Thomas–Fermi fluid at a given  $\lambda$ . The characteristic length  $\ell$  converts the volume energy to a surface energy. Symbols correspond to the same densities as in the main figure, color coding denotes different  $\lambda$  as in (a).

*Wetting transition* — Having assessed our effective simulation strategy, we now turn to the thermodynamically relevant case of the wetting of an ionic liquid at metal surfaces. Molten NaCl is modeled using

charged particles  $\pm 1e$  that interact via a Born–Mayer–Huggins potential [21] (details can be found in the *Supplemental Material*). To prevent mixing of the Thomas–Fermi fluid/charged system, a reflective wall of thickness  $e = 0.2$  nm is positioned between the two subsystems. Fig. 4(a) shows the density profiles  $\rho(z)$  for the salt and Thomas–Fermi fluid for different  $\lambda$  (which is modified by tuning  $q_{\text{TF}}$ ). A crossover is observed upon decreasing  $\lambda$ ; while the salt is depleted at the insulating interface, a marked ion density peak appears under metallic conditions (in contrast, the density profile for the Thomas–Fermi fluid is nearly unaffected by  $\lambda$ ). This behavior suggests that the system undergoes a wetting transition upon changing the dielectric/metallic nature of the confining medium (perfect wetting/non-wetting for metal/insulator, respectively).

The observed wetting transition was characterized by measuring the surface tension of the liquid salt confined at a constant density within surfaces made of a metallic medium with a screening length  $\lambda$  via the Irving–Kirkwood formula:  $\gamma(\lambda) = L_z/2\langle P_N - P_T \rangle$  where the terms in bracket are the average normal and tangential pressures,  $L_z$  is the box length in the  $z$  direction and the factor 2 accounts for the two interfaces in the slit geometry. We considered the salt in its liquid ( $l$ ) and gas ( $g$ ) states in contact with the metal ( $m$ ) and estimated for various  $\lambda$  the surface tension difference normalized to the gas-liquid surface tension,  $\Delta\gamma(\lambda)/\gamma_{\text{gl}} = [\gamma_{\text{gm}}(\lambda) - \gamma_{\text{lm}}(\lambda)]/\gamma_{\text{gl}}$ . In practice,  $\gamma_{\text{lg}}$  was assumed to correspond to the liquid-wall surface at the insulating surface, i.e.  $\gamma_{\text{lg}} \sim \gamma_{\text{lw}}(\infty)$  (this approximation does not affect the discussion below as  $\gamma_{\text{lg}}$  is used for normalization only). As shown in Fig. 4(b), upon switching the surfaces from insulating to metallic, the confined salt undergoes a continuous transition from non-wetting or partially wetting [ $\Delta\gamma(\lambda)/\gamma_{\text{gl}} \leq 1$ ] to perfectly wetting [ $\Delta\gamma(\lambda)/\gamma_{\text{gl}} > 1$ ]. For imperfect metals with  $\lambda \gtrsim 0.1$  nm, the spreading parameter  $S = \gamma_{\text{gm}} - \gamma_{\text{lm}} - \gamma_{\text{lg}} < 0$  and the contact angle  $\theta$  can be inferred from Young equation  $\Delta\gamma/\gamma_{\text{lg}} = \cos\theta$  (with  $\cos\theta < 0$  and  $> 0$  for non-wetting and partially wetting, respectively). For metals with  $\lambda \lesssim 0.1$  nm,  $S \geq 0$  so that the system becomes perfectly wetting with a liquid film spreading over the metal surface. As shown in the inset of Fig. 4(b), the change in  $\Delta\gamma$  between the insulator and metal is found to scale with the liquid/gas density contrast:

$$\Delta(\Delta\gamma(\lambda)) = \Delta\gamma(\lambda) - \Delta\gamma(\infty) \sim (\rho_l - \rho_g)\alpha(\lambda) \sim \rho_l\alpha(\lambda) \quad (4)$$

where  $\rho_l \gg \rho_g$  was assumed in the second equality. As expected from the Thomas–Fermi model, the inset in Fig. 4(b) shows that  $\alpha(\lambda) \sim U_{\lambda}^{\text{CI}}$  as the charge interaction with the induced density distributions (including the charge image) is dominating the surface energy excess. This important finding provides a microscopic picture for recent experimental results in which capillary

freezing and wetting of an ionic liquid was found to be promoted by metal surfaces [11, 22]. In particular, these authors showed that the freezing point shift upon varying  $\lambda$  could be rationalized by assuming that the difference between the liquid/wall and crystal/wall surface tensions scales with the density difference between the crystal and liquid [11].

In this Letter, we developed a classical molecular simulation strategy that allows considering the confinement within any material ranging from perfect metal to insulator. This approach, which does not require to input any given geometry/molecular structure for the confining material, describes in an effective fashion electrostatic screening within confined/vicinal fluids. After straightforward integration into an existing simulation package, this method offers a useful framework to investigate the behavior of dipolar and charged fluids in porous materials made up of any material with imperfect dielectric/metal properties. Beyond practical implications, we also unraveled a non-wetting/wetting crossover in nanoconfined liquids as the confining surfaces vary from insulator to perfect metal. This raises new challenging questions on the complex behavior of charged systems in the vicinity or confined within surfaces with important applications such as electrowetting/switching for energy storage, lubrication, catalysis, etc.

We acknowledge V. Kaiser for his help with the Thomas–Fermi model and computation time through CIMENT infrastructure (Rhône-Alpes CPER07\_13 CIRA) and Equip@Meso project (ANR-10-EQPX-29-01).

*Chem. C* **119**, 22445 (2015).

- [11] J. Comtet, A. Niguès, V. Kaiser, B. Coasne, L. Bocquet, and A. Siria, *Nat. Mater.* **16**, 634 (2017).
- [12] N. W. Ashcroft and N. D. Mermin, *Solid State Physics* (Holt, Rinehart and Winston, 1976).
- [13] A. P. dos Santos, M. Girotto, and Y. Levin, *J. Chem. Phys.* **147**, 184105 (2017).
- [14] J. I. Siepmann and M. Sprik, *J. Chem. Phys.* **102**, 511 (1995).
- [15] S. K. Reed, O. J. Lanning, and P. A. Madden, *The Journal of Chemical Physics* **126**, 084704 (2007).
- [16] S. Tyagi, M. Süzen, M. Sega, M. Barbosa, S. S. Kantorovich, and C. Holm, *J. Chem. Phys.* **132**, 154112 (2010).
- [17] A. Arnold, K. Breitsprecher, F. Fahrenberger, S. Kesselheim, O. Lenz, and C. Holm, *Entropy* **15**, 4569 (2013).
- [18] T. D. Nguyen, H. Li, D. Bagchi, F. J. Solis, and M. Olvera de la Cruz, *Computer Physics Communications* **241**, 80 (2019).
- [19] G. M. Torrie and J. P. Valleau, *Journal of Electroanalytical Chemistry and Interfacial Electrochemistry* **206**, 69 (1986).
- [20] S. Plimpton, *J. Comput. Phys.* **117**, 1 (1995).
- [21] J. Anwar, D. Frenkel, and M. G. Noro, *J. Chem. Phys.* **118**, 728 (2002).
- [22] A. Lainé, A. Niguès, L. Bocquet, and A. Siria, *Phys. Rev. X* **accepted** (2019).

\* [alexander.schlaich@univ-grenoble-alpes.fr](mailto:alexander.schlaich@univ-grenoble-alpes.fr)

† [benoit.coasne@univ-grenoble-alpes.fr](mailto:benoit.coasne@univ-grenoble-alpes.fr)

- [1] L. Bocquet and E. Charlaix, *Chem. Soc. Rev.* **39**, 1073 (2010).
- [2] M. V. Fedorov and A. A. Kornyshev, *Chem. Rev.* **114**, 2978 (2014).
- [3] V. Kaiser, J. Comtet, A. Niguès, A. Siria, B. Coasne, and L. Bocquet, *Faraday Discuss.* **199**, 129 (2017).
- [4] T. Dufils, L. Scalfi, B. rotenberg, and M. Salanne, ArXiv191013341 Cond-Mat (2019), [arXiv:1910.13341 \[cond-mat\]](https://arxiv.org/abs/1910.13341).
- [5] D. M. Newns, *J. Chem. Phys.* **50**, 4572 (1969); J. C. Inkson, *J. Phys. C: Solid State Phys.* **6**, 1350 (1973); A. A. Kornyshev, A. I. Rubinshtein, and M. A. Vorotyntsev, *Phys. Status Solidi B* **84**, 125 (1977).
- [6] N. B. Luque and W. Schmickler, *Electrochimica Acta* **71**, 82 (2012); A. A. Kornyshev, N. B. Luque, and W. Schmickler, *J. Solid State Electrochem* **18**, 1345 (2014).
- [7] R. R. Netz, *Phys. Rev. E* **60**, 3174 (1999).
- [8] A. A. Lee and S. Perkin, *J. Phys. Chem. Lett.* **7**, 2753 (2016).
- [9] D. Bedrov, J.-P. Piquemal, O. Borodin, A. D. MacKerell, B. Roux, and C. Schröder, *Chem. Rev.* **119**, 7940 (2019).
- [10] K. Breitsprecher, K. Szuttor, and C. Holm, *J. Phys.*

**Wetting transition of ionic liquids at metal surfaces: A computational approach to electronic screening using a virtual Thomas-Fermi fluid**  
**SUPPLEMENTAL MATERIAL**

Alexander Schlaich,<sup>1,\*</sup> Dongliang Jin,<sup>1</sup> Lyderic Bocquet,<sup>2</sup> and Benoit Coasne<sup>1,†</sup>

<sup>1</sup> *Univ. Grenoble Alpes, CNRS, LIPhy, 38000 Grenoble, France*

<sup>2</sup> *Laboratoire de Physique de l'Ecole Normale Supérieure, CNRS, Université PSL, Sorbonne Université, Sorbonne Paris Cité, Paris, France*

**CONTENTS**

I. Electrostatic interactions close to a Thomas–Fermi substrate	1
A. Thomas Fermi screening	1
B. Green function of a charge close to a Thomas–Fermi interface	3
C. One-body interaction: A single point charge close to a Thomas–Fermi interface	5
D. Two-body interaction: Two point charges close to a Thomas–Fermi interface	7
II. Thomas–Fermi energy for a two-dimensional ionic crystal	10
III. Simulation details	13
IV. Influence of interaction potentials, salt slab width and Thomas–Fermi layer width	14
V. Energy decomposition from simulation reruns	15
VI. General connection to screening in linear dielectric media	17
References	19

**I. ELECTROSTATIC INTERACTIONS CLOSE TO A THOMAS–FERMI SUBSTRATE**

**A. Thomas Fermi screening**

In classical electrostatic theory, a point charge brought in front of a conducting solid is treated by considering an ideal metal where the induced electric field is perfectly screened in an infinitesimally

---

<sup>\*</sup> [alexander.schlaich@univ-grenoble-alpes.fr](mailto:alexander.schlaich@univ-grenoble-alpes.fr)

<sup>†</sup> [benoit.coasne@univ-grenoble-alpes.fr](mailto:benoit.coasne@univ-grenoble-alpes.fr)

small surface layer [1]. The corresponding interaction potential of the point charge with the metal can then be obtained using, as a purely mathematical tool, the method of image charges (i.e. the potential of an equal charge of opposite sign mirrored by the surface). At the molecular scale, this macroscopic description of perfect screening breaks down as the quantum mechanical nature of electrons leads to delocalization [2]. More in detail, the latter implies that the screening lengthscale cannot be infinitesimally small, but rather the interactions are screened over a typical lengthscale  $\lambda$ .

The simplest theory to describe screening at a finite wavevector  $k_{\text{TF}} = \lambda^{-1}$  was introduced independently by Thomas [3] and Fermi [4] who treated the electrons as a non-interacting homogeneous gas. The latter approximation neglects the correlations of electronic wavefunctions using a mean-field treatment. In this case, the chemical potential  $\mu$  of the electrons equals (in the zero temperature limit) the Fermi energy  $E_F$  and is directly related to the electron density  $n_0$  inside the metal (see e.g. Ref. [5] for a derivation),

$$\mu = E_F = \frac{\hbar^2}{2m_e} (3\pi^2 n_0)^{2/3}, \quad (\text{S1})$$

where  $\hbar$  is the reduced Planck constant and  $m_e$  the electron mass.

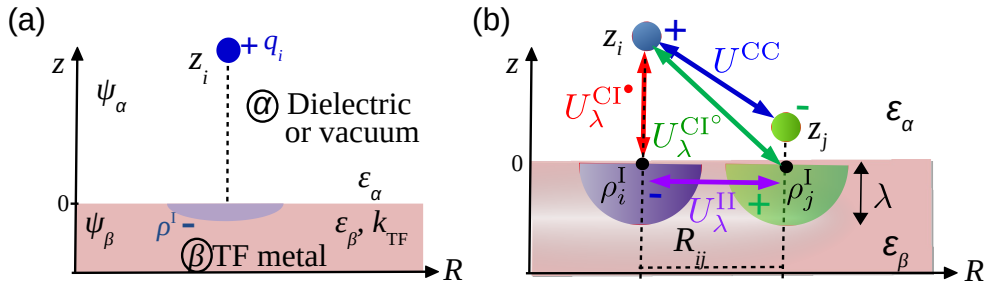


Figure S1. Electrostatic interactions at a metal/dielectric interface. (a) A single point charge  $q_i$  in the dielectric medium  $\alpha$  induces a charge distribution  $\rho^I$  inside the metal  $\beta$  (but located close to the interface). (b) Decomposition of the total energy  $U_\lambda$  for two charges  $i$  and  $j$  into one- and two-body terms.

Let us now consider an interfacial system consisting of a dielectric medium (denoted by  $\alpha$ ) in contact with a metal (denoted by  $\beta$ ), see Fig. S1(a). Any charge brought close to the metal will disturb the local density distribution  $n_0(\mathbf{r})$  by generating an electrostatic potential,  $\Psi_\beta$ , within the metal. The induced charge density inside the metal,  $\rho^I(\mathbf{r})$ , results from a competition between (1) the energy reduction due to the screening of the electrostatic potential  $\Psi_\beta$  generated by the external charge and (2) the energy cost of localizing the induced charge  $\rho^I$  [6],

$$\rho^I(\mathbf{r}) = -e [n_0(\mu - e\Psi_\beta(\mathbf{r})) - n_0(\mu)]. \quad (\text{S2})$$

Equation (S2) is the non-linear Thomas–Fermi (TF) equation and an expansion to the first order yields the linearized TF equation,

$$\rho^I(\mathbf{r}) = -e^2 \frac{\partial n_0}{\partial \mu} \Psi_\beta(\mathbf{r}). \quad (\text{S3})$$

As shown in Section VI, in analogy to the linear dielectric theory, it is convenient to define the proportionality factor as the Thomas–Fermi wavevector,

$$k_{\text{TF}}^2 = \frac{e^2}{\varepsilon_0} \frac{\partial n_0}{\partial \mu}. \quad (\text{S4})$$

For temperatures small compared to the Fermi temperature, i.e.  $T \ll T_F = \mathcal{E}_F/k_B$ ,  $\partial n_0/\partial \mu$  is directly given by the density of states  $\mathcal{D}(\mathcal{E}_F)$  at the Fermi level  $\mathcal{E}_F$  of the material  $\beta$  [7]. Taking into account polarization effects via  $\varepsilon_\beta$ , the TF wavevector thus follows as

$$k_{\text{TF}} = \lambda^{-1} = \frac{e^2}{\varepsilon_\beta \varepsilon_0} \mathcal{D}(\mathcal{E}_F) = \frac{e^2}{\varepsilon_\beta \varepsilon_0} \frac{1}{2\pi^2} = \sqrt{m_e e^2 k_F / (\varepsilon_\beta \varepsilon_0 \hbar^2 \pi^2)}, \quad (\text{S5})$$

where  $k_F = (\mathcal{D}(\mathcal{E}_F)/(3\pi^2))^1/3$  is the Fermi wave vector and

$$\mathcal{D}(\mathcal{E}_F) = \frac{1}{2\pi^2} \left( \frac{2m}{\hbar^2} \right)^{3/2} \sqrt{\mathcal{E}_F} \quad (\text{S6})$$

is the density of states of a Fermi gas at the Fermi energy  $\mathcal{E}_F = \hbar^2(3\pi^2 n_0)^{2/3}/(2m_e)$ . Within the nearly free electron model, the charge density is roughly equal to the number density of atoms in the metal  $n_0 \sim 10\text{--}100 \text{ nm}^{-3}$ . Thus, at room temperature, the relation  $T \ll T_F \sim 10^5\text{--}10^6 \text{ K}$  is fully justified.  $k_{\text{TF}}$  is a quantity that characterizes the strength of the screening (see Section VI) which, according to Eq. (S5), increases with  $\mathcal{D}(\mathcal{E}_F)$ . An increased density of states permits the electron density to vary more with a lesser effect on the chemical potential of the local Fermi liquid. This reduces the cost of screening the external potential and, thus, results in a smaller screening length  $\lambda$ .

## B. Green function of a charge close to a Thomas–Fermi interface

The Green function of a charge  $q_i$  at a distance  $z_i$  from a TF interface allows obtaining the potential energy [Fig. S1(a)]. Due to the symmetry, we define  $\Psi(\mathbf{r}) = \Psi(z, R)$  in cylindrical coordinates. The derivation presented below largely follows the steps presented in Ref. [8]. The charge  $q_i$  is located inside an insulator ( $\varepsilon_\alpha \neq 1$ ) or vacuum ( $\varepsilon_\alpha = 1$ ) at a position  $\mathbf{r}_i$  with a coordinate  $z_i$  along the  $z$ -direction normal to the surface and a radial position  $R_i = 0$  in the  $xy$ -plane, while the TF substrate is located in the half-space  $z < 0$ , see Fig. S1(a).

The Green function for the upper half-space  $z > 0$  is obtained from Poisson equation,

$$\nabla^2 \Psi_\alpha(\mathbf{r}) = \frac{\rho(\mathbf{r})}{\varepsilon_0 \varepsilon_\alpha} = -\frac{q_i \delta(\mathbf{r} - \mathbf{r}_i)}{\varepsilon_0 \varepsilon_\alpha} \quad (\text{S7})$$

$$\rightarrow \nabla^2 \Psi_\alpha(z, R) = -\frac{q_i \delta(z - z_i) \delta(R)}{2\pi \varepsilon_0 \varepsilon_\alpha R}, \quad (\text{S8})$$

where we have used the Dirac function in cylindrical coordinates,  $\delta(\mathbf{r} - \mathbf{r}_i) = \delta(R - R_i)/2\pi R$ . Inserting Eq. (S4) into Eq. (S3) and using Poisson equation given in Eq. (S7), the linearized TF equation can be recast as

$$\nabla^2 \Psi_\beta(z, R) - k_{\text{TF}}^2 \Psi_\beta(z, R) = 0. \quad (\text{S9})$$

Equations (S8) and (S9) describe the electrostatic potential  $\Psi$  in the insulator  $\alpha$  and the metal  $\beta$ , respectively. The Green function in Eqs. (S8) and (S9) can be solved for via Hankel integral transformation of first order [9]:  $\Psi(z, K) = \int dR R J_0(KR) \Psi(z, R)$  where  $R$  is the radial component along the surface [see Fig. S1(a)],  $K$  is the corresponding radial wavevector and  $J_0$  is the Bessel function of first kind. Hankel transformation applied to Eqs. (S8) and (S9) yields

$$(\partial_{zz} - K^2) \Psi_\alpha = -\frac{q_1 \delta(z - z_i)}{2\pi \varepsilon_0 \varepsilon_\alpha} \quad (\text{S10})$$

$$(\partial_{zz} - \kappa^2) \Psi_\beta = 0, \quad (\text{S11})$$

where we have used  $\kappa_{\text{TF}}^2 = K^2 + k_{\text{TF}}^2$  to simplify notation.

Using that the potential must vanish in all directions at infinity and the boundary condition at the surface given by the continuity of the potential  $\Psi_\alpha(z_i; z = 0_+) = \Psi_\beta(z_i; z = 0_-)$  and the electric displacement field  $\varepsilon_\alpha[\partial_z \Psi_\alpha](z_i; z = 0_+) = \varepsilon_\beta[\partial_z \Psi_\beta](z_i; z = 0_-)$ , the Green functions read (as derived e.g. in Refs. [10–13])

$$\begin{aligned} \Psi_\alpha^>(z_i; z > z_i, K) &= \frac{q_1}{4\pi \varepsilon_0 \varepsilon_\alpha K} \left[ e^{+Kz_i} + \frac{\varepsilon_\alpha K - \varepsilon_\beta \kappa_{\text{TF}}}{\varepsilon_\alpha K + \varepsilon_\beta \kappa_{\text{TF}}} e^{-Kz_i} \right] e^{-Kz} \\ \Psi_\alpha^<(z_i; z < z_i, K) &= \frac{q_1}{4\pi \varepsilon_0 \varepsilon_\alpha K} \left[ e^{+Kz} + \frac{\varepsilon_\alpha K - \varepsilon_\beta \kappa_{\text{TF}}}{\varepsilon_\alpha K + \varepsilon_\beta \kappa_{\text{TF}}} e^{-Kz} \right] e^{-Kz_i} \end{aligned} \quad (\text{S12})$$

$$\Psi_\beta(z_i; z, K) = \frac{q_1 e^{-Kz_i}}{2\pi \varepsilon_0} \frac{e^{\kappa_{\text{TF}} z}}{\varepsilon_\alpha K + \varepsilon_\beta \kappa_{\text{TF}}}. \quad (\text{S13})$$

The first term inside the brackets of Eq. (S12) is the potential generated by the point charge  $q_i$ , whereas the second term corresponds to the potential generated by the induced charge in the TF substrate. We explicitly kept in Eqs. (S12) and (S13) the parametric dependence on the distance  $z_i$ .

### C. One-body interaction: A single point charge close to a Thomas–Fermi interface

Let us consider an isolated point charge  $i$  at a distance  $z_i$  from a TF metal, see Fig. S1(a). For an ideal metal  $\lambda \rightarrow \infty$ , the electrostatic energy can be obtained using the method of image charges as  $U_{\infty}^{\text{CI}\bullet} = -q_i^2/(16\pi\epsilon_0\epsilon_{\alpha}z_i)$ , which is equal to half of the energy that a real pair of interacting charges would have [14]. We recall that the symbol  $\bullet$  refers to the interaction of a charge with its image in the metal, see main text. For a TF metal characterized by a finite screening length  $\lambda$ , we follow the derivation in Ref. [8] and compute the electrostatic energy via the volume integral of the product of the charge density and the potential,  $U_{\lambda}^{\text{CI}\bullet} = \int d\mathbf{r}\rho(\mathbf{r})\Psi(\mathbf{r})$ . The latter integral has to be taken over the full space in  $z$  and thus the corresponding solutions  $\Psi_{\alpha}$  and  $\Psi_{\beta}$  in Eqs. (S12) and (S13) have to be taken for  $z > 0$  and  $z < 0$ , respectively. The total charge density  $\rho(\mathbf{r}) = \rho^{\bullet}(\mathbf{r}) + \rho^{\text{I}}(\mathbf{r})$  follows from the sum of the point charge,  $\rho^{\bullet}(\mathbf{r}) = q_i\delta(\mathbf{r} - \mathbf{r}_i)$  and the induced charge density  $\rho^{\text{I}}(\mathbf{r})$ .

By combining Eqs. (S3), (S4) and (S13), the induced charge density  $\rho^{\text{I}}$  as derived from the TF equation is proportional to the electrostatic potential in the metal,

$$\rho^{\text{I}}(z_i; z, K) = -\epsilon_0\epsilon_{\beta}k_{\text{TF}}^2\Psi_{\beta}(z_i; z, K) = -\frac{\epsilon_{\beta}k_{\text{TF}}^2q_1e^{-Kz_i}}{2\pi(\epsilon_{\alpha}K + \epsilon_{\beta}\kappa_{\text{TF}})}e^{\kappa_{\text{TF}}z}. \quad (\text{S14})$$

Note that Eqs. (S13) and (S14) are defined only in the lower half-space  $z < 0$ . Upon applying the Plancherel theorem and the inverse Hankel transform  $\Psi(z, R) = \int dKKJ_0(KR)\Psi(z, K)$ , the one-body energy reads [8]

$$\begin{aligned} U_{\lambda}^{\text{CI}\bullet}(z_i) &= \frac{1}{2} \int_{-\infty}^{\infty} dz \int_0^{\infty} 2\pi R dR [\rho^{\text{I}}(z_i; z, R)\Psi_{\beta}(z_i; z, R) + \rho^{\bullet}(z_i; z, R)\Psi_{\alpha}(z_i; z, R)] \\ &= \pi \int_{-\infty}^{\infty} dz \int_0^{\infty} dKK [\rho^{\text{I}}(z_i; z, K)\Psi_{\beta}(z_i; z, K) + \rho^{\bullet}(z_i; z, K)\Psi_{\alpha}(z_i; z, K)] \\ &=: U_{\text{I}}^{\text{CI}\bullet}(z_i) + U_{\bullet}^{\text{CI}\bullet}(z_i), \end{aligned} \quad (\text{S15})$$

The first term defined by the right hand side of Eq. (S15) is the potential energy  $U_{\text{I}}^{\text{CI}\bullet}$  of the induced charge, i.e. the energy needed to induce the charge density  $\rho^{\text{I}}$  in the metal. The second term is the potential energy  $U_{\bullet}^{\text{CI}\bullet}$  of the point charge in front of the Thomas–Fermi substrate. Inserting Eq. (S14) and using that the induced charge  $\rho^{\text{I}}$  is only defined in the half-space  $z < 0$ , one obtains

$$\begin{aligned} U_{\text{I}}^{\text{CI}\bullet}(z_i) &= -\pi\epsilon_0\epsilon_{\beta}k_{\text{TF}}^2 \int_{-\infty}^0 dz \int_0^{\infty} dKK [\Psi_{\beta}(z_i; z, K)]^2 \\ &= -\frac{q_i^2}{8\pi\epsilon_0\epsilon_{\beta}}k_{\text{TF}}^2 \int_0^{\infty} dKK \frac{e^{-2Kz_i}}{\left((\epsilon_{\alpha}/\epsilon_{\beta})K + \sqrt{K^2 + k_{\text{TF}}^2}\right)^2 \sqrt{K^2 + k_{\text{TF}}^2}}. \end{aligned} \quad (\text{S16})$$

By substituting the integration variable with the dimensionless variable  $\xi = Kz_i$ , the latter can be brought into a slightly more familiar form [8],

$$U_I^{CI^\bullet}(z_i) = -\frac{q_1^2}{16\pi\varepsilon_0\varepsilon_\beta} \int_0^\infty d\xi \frac{2(k_{TF}z_i)^2\xi e^{-2\xi}}{\left((\varepsilon_\alpha/\varepsilon_\beta)\xi + \sqrt{\xi^2 + (k_{TF}z_i)^2}\right)^2 \sqrt{\xi^2 + (k_{TF}z_i)^2}} \\ =: -\frac{q_1^2}{16\pi\varepsilon_0\varepsilon_\beta} \mathcal{I}_I(z_i, k_{TF}), \quad (S17)$$

where the right hand side defines the integral  $\mathcal{I}_I$ .

We now consider the second term in Eq. (S15). In cylindrical coordinates, the charge density located on the axis  $R = 0$  reads as  $\rho^\bullet(z) = q_i\delta(z - z_i)/(2\pi)$ . Therefore, the two cases  $\Psi_\alpha^>$  and  $\Psi_\alpha^<$  in Eq. (S12) are equal upon integration in  $z$  of  $\rho^\bullet\Psi_\alpha$  in Eq. (S15). For instance, using the expression  $\Psi_\alpha^>$  one obtains

$$U_\bullet^{CI^\bullet}(z_i) = \pi \int_{-\infty}^\infty dz \int_0^\infty dKK \frac{q_1\delta(z - z_i)}{2\pi} \frac{q_1}{4\pi\varepsilon_0\varepsilon_\alpha K} \left[ e^{+Kz_i} + \frac{\varepsilon_\alpha K - \varepsilon_\beta \kappa_{TF}}{\varepsilon_\alpha K + \varepsilon_\beta \kappa_{TF}} e^{-Kz_i} \right] e^{-Kz} \\ = \frac{q_1^2}{8\pi\varepsilon_0\varepsilon_\alpha} \int_0^\infty dK \left[ 1 - \frac{\varepsilon_\beta \sqrt{K^2 + k_{TF}^2} - \varepsilon_\alpha K}{\varepsilon_\beta \sqrt{K^2 + k_{TF}^2} + \varepsilon_\alpha K} e^{-2Kz_i} \right] \quad (S18)$$

The first term corresponds to the diverging self-energy of any point charge. In line with the treatment in classical electrostatics [1], we omit this static part in the following, as it simply corresponds to a constant self-contribution. Again, substituting the integration variable by  $\xi = Kz_i$  yields

$$U_\bullet^{CI^\bullet}(z_i) = \frac{q_1^2}{8\pi\varepsilon_0\varepsilon_\alpha z_i} \int_0^\infty d\xi \frac{\sqrt{\xi^2 + (k_{TF}z_i)^2} - (\varepsilon_\alpha/\varepsilon_\beta)\xi}{\sqrt{\xi^2 + (k_{TF}z_i)^2} + (\varepsilon_\alpha/\varepsilon_\beta)\xi} e^{-2\xi} \\ = \frac{q_1^2}{16\pi\varepsilon_0\varepsilon_\alpha z_i} \left[ \int_0^\infty d\xi \frac{4(\varepsilon_\alpha/\varepsilon_\beta)\xi}{\sqrt{\xi^2 + (k_{TF}z_i)^2} + \varepsilon_\alpha/\varepsilon_\beta\xi} e^{-2\xi} - 1 \right] \\ =: -\frac{q_1^2}{16\pi\varepsilon_0\varepsilon_\alpha z_i} [1 - \mathcal{I}_\bullet(z_i, k_{TF})]. \quad (S19)$$

The integrals  $\mathcal{I}_I$  and  $\mathcal{I}_\bullet$  defined above can be obtained numerically with high accuracy using common routines such as QUADPACK. In practice, we employ the latter through Python's `scipy.integrate.quad` interface to obtain the numerical results such as those shown in Fig. S2(a). Asymptotic analysis reveals that  $\mathcal{I}_I$  vanishes both in the ideal metal and insulator limits,  $k_{TF} = 1/\lambda \rightarrow \infty$  and  $k_{TF} \rightarrow 0$ , respectively.  $\mathcal{I}_\bullet$  vanishes in the ideal metal limit and goes to unity for the perfect insulator,  $\varepsilon_\beta = \varepsilon_\alpha = 1$ . This directly reveals that, without dielectric contrast, as expected, the energy of a single point charge at a perfect metal interface is half of the equivalent energy at an insulator surface. Figure S2(b) shows as an example the resulting energy  $U^{CI^\bullet}$  and its

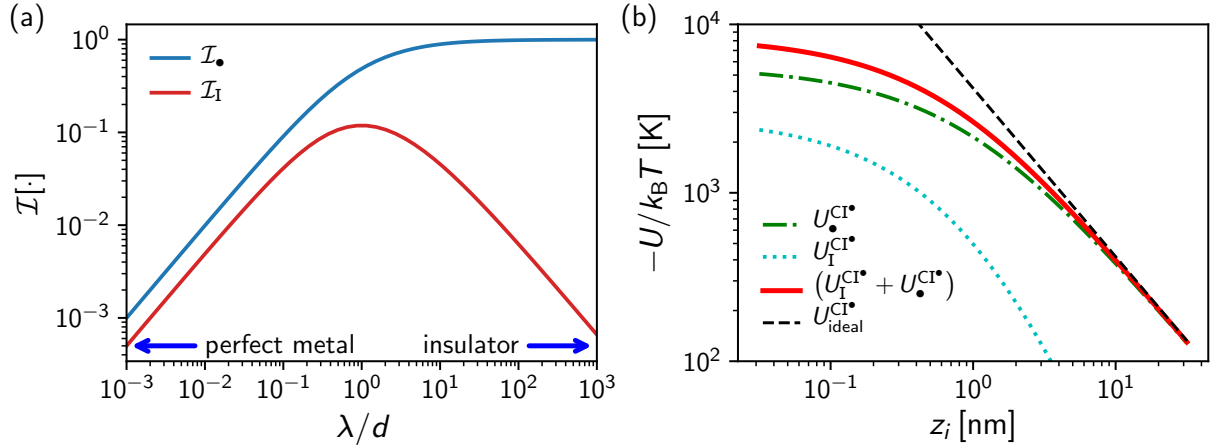


Figure S2. Numerical results for the one-body energy: (a) Dependence of the integrals  $\mathcal{I}$  on the dimensionless screening length  $\lambda/z_i = k_{\text{TF}}z_i$ . (b) One-body electrostatic energy  $-U_\lambda^{\text{CI}*}$  and its contributions according to Eqs. (S17) and (S19) for a fixed screening length  $\lambda = 1 \text{ nm}$ . The dashed black line shows the perfect metal limit.

contributions for  $\lambda = 1 \text{ nm}$  compared to the ideal metal,  $U_\infty^{\text{CI}*} = q_1^2/(16\pi\varepsilon_0\varepsilon_\alpha z_i)$ . As the implicit dielectric constants in our simulations are  $\varepsilon_\beta = \varepsilon_\alpha = 1$ , we fix this ratio for all data reported here. Note that for numerical reasons the unit of the inverse length  $\xi = Kz_i$  in Eqs. (S17) and (S19) should be chosen such that  $\lambda/z_i \sim 1$

#### D. Two-body interaction: Two point charges close to a Thomas–Fermi interface

Let us now consider two point charges  $i$  and  $j$  in front of a TF substrate as depicted in Fig. S1(b). As discussed in the main text, we decompose the total energy into the following contributions,

$$U_\lambda(z_i, z_j, R_{ij}) = U^{\text{CC}}(r_{ij}) + U_\lambda^{\text{CI}}(z_i, z_j, R_{ij}) + U_\lambda^{\text{II}}(z_i, z_j, R_{ij}), \quad (\text{S20})$$

where  $z_i$  and  $z_j$  are the distances normal to the surface,  $R_{ij}$  is the in-plane separation and  $r_{ij} = \sqrt{R_{ij}^2 + (z_i - z_j)^2}$  is the distance between the charges. In the following, we discuss the individual contributions and the numerical solution procedures employed.

**Direct Coulomb interaction:**  $U^{\text{CC}}$  denotes the direct Coulomb charge–charge interaction between the point charges,  $U^{\text{CC}} = q_i q_j / (4\pi\varepsilon_0\varepsilon_\alpha r_{ij})$ . In the general case of a fluid consisting of  $N$  charges, the corresponding Coulomb energy of the charge  $i$  reads as

$$U_i^{\text{CC}} = \frac{q_i}{8\pi\varepsilon_0\varepsilon_\alpha} \sum_{j \neq i}^N \frac{q_j}{r_{ij}}, \quad (\text{S21})$$

where the additional factor  $1/2$  stems from the fact that the energy  $U^{\text{CC}}$  contributes to both particles  $i$  and  $j$ . To simplify notation, in the following, we skip the index  $i$  for the total energy of particle  $i$  and refer to the sum  $j \neq i$  whenever no indices  $(ij)$  are specified. This approach is equivalent to considering the statistical average of a particle in a fluid,  $U^{\text{CC}} = \langle U_i^{\text{CC}} \rangle_N$ .

A special case emerges when a periodic crystal of point charges  $q_i = -q_j = q$  is considered. In this case, Eq. (S21) can be recast in terms of the Madelung constant  $\mathcal{M}$ ,

$$U^{\text{CC}} = -\frac{q^2}{8\pi\epsilon_0\epsilon_\alpha a_0} \mathcal{M}. \quad (\text{S22})$$

Here,  $a_0$  is the nearest neighbor distance (which corresponds to half of the crystal unit cell) and  $\mathcal{M}$  depends on the dimension of the crystal as  $\mathcal{M} = 2\ln 2$  in one dimension,  $\mathcal{M} \approx 1.61554$  in two dimensions [15] and  $\mathcal{M} \approx 1.747564594$  in three dimensions [16].

**Charge–image interaction  $U_\lambda^{\text{CI}}$ :** We decompose the charge–image interaction of particle  $i$  interacting with particle  $j$  at the TF interface according to  $U_\lambda^{\text{CI}} = U_\lambda^{\text{CI}^\bullet}(z_i) + U_\lambda^{\text{CI}^\circ}(z_i, z_j, R_{ij})$ , where  $U_\lambda^{\text{CI}^\bullet}$  is the one-body term given by Eq. (S15) and  $U_\lambda^{\text{CI}^\circ}$  the electrostatic energy of charge  $i$  interacting with the induced charge density  $\rho^{\text{I}}(z_j; z, R)$  due to the charge  $j$ . Making use of symmetry, the only relevant variable in the  $R$ -direction is the projected particle distance  $R_{ij}$ , see Fig. S1(b).  $U_\lambda^{\text{CI}^\circ}$  is obtained from the convolution of the induced charge of  $j$  and the electrostatic potential  $\Psi_\beta$  due to charge  $i$  in the metal, i.e.  $U_\lambda^{\text{CI}^\circ} = \int d\mathbf{r} \Psi_\beta(\mathbf{r}_i; \mathbf{r}) \rho^{\text{I}}(\mathbf{r}_j; \mathbf{r})$ . This leads to

$$\begin{aligned} U_\lambda^{\text{CI}^\circ}(z_i, z_j, R_{ij}) &= \int_{-\infty}^0 dz \int_0^\infty 2\pi R_{ij} dR_{ij} \Psi_\beta(z_i; z, R_{ij}) \rho^{\text{I}}(z_j; z, R_{ij}) \\ &= 2\pi \int_{-\infty}^0 dz \int_0^\infty dK K J_0(KR_{ij}) \Psi_\beta(z_i; z, K) \rho^{\text{I}}(z_j; z, K). \end{aligned} \quad (\text{S23})$$

Using Eqs. (S13) and (S14), this yields

$$\begin{aligned} U_\lambda^{\text{CI}^\circ}(z_i, z_j, R_{ij}) &= -\frac{q_i q_j}{2\pi\epsilon_0} \int_{-\infty}^0 dz \int_0^\infty dK K J_0(KR_{ij}) \frac{\epsilon_\beta k_{\text{TF}}^2}{(\epsilon_\alpha K + \epsilon_\beta \kappa_{\text{TF}})^2} e^{-K(z_i + z_j)} e^{2\kappa_{\text{TF}} z} \\ &= -\frac{q_i q_j}{4\pi\epsilon_0} \int_0^\infty dK J_0(KR_{ij}) \frac{K \epsilon_\beta k_{\text{TF}}^2}{\sqrt{K^2 + k_{\text{TF}}^2} (\epsilon_\alpha K + \epsilon_\beta \sqrt{K^2 + k_{\text{TF}}^2})^2} e^{-K(z_i + z_j)}. \end{aligned} \quad (\text{S24})$$

Equation (S24) can be integrated numerically as discussed above.

**Image–image interaction  $U_\lambda^{\text{II}}$ :** The resulting expressions for the image–image interactions are more involved. The general expression for the energy of the image charge of particle  $i$  in the electrostatic potential induced by particle  $j$  follows from the convolution

$$U_\lambda^{\text{II}}(\mathbf{r}_i, \mathbf{r}_j) = \int d\mathbf{r} \rho^{\text{I}}(\mathbf{r}_i; \mathbf{r}) \Psi_\beta(\mathbf{r}_j; \mathbf{r}). \quad (\text{S25})$$

Due to the spatial extension of the induced charges, the volume integral cannot be transformed into cylindrical coordinates conveniently. We thus use cartesian coordinates and, to simplify notation, we locate the charge  $i$  at the origin,  $\mathbf{r}_i = (0, 0, z_i)$  and the charge  $j$  at distance  $R_{ij}$  on the  $x$ -axis,  $\mathbf{r}_j = (R_{ij}, 0, z_j)$ ,

$$U_{\lambda}^{\text{II}}(z_i, z_j, R_{ij}) = \frac{1}{2} \int dx dy dz \rho^{\text{I}}(z_i; x, y, z) \Psi_{\beta}(z_j, R_{ij}; x, y, z). \quad (\text{S26})$$

This allows us to use the previously derived expression for the induced charge given in Eq. (S14), which upon inverse Hankel transform reads

$$\rho^{\text{I}}(z_i; x, y, z) = -\frac{\varepsilon_{\beta} k_{\text{TF}}^2 q_i}{2\pi} \int_0^{\infty} dK J_0(Kr_{\parallel}) \frac{e^{-Kz_i}}{\varepsilon_{\alpha} K + \varepsilon_{\beta} \sqrt{K^2 + k_{\text{TF}}^2}} e^{\sqrt{K^2 + k_{\text{TF}}^2} z}, \quad (\text{S27})$$

where  $r_{\parallel} = \sqrt{x^2 + y^2}$ . Similarly, upon introducing  $R_{\parallel} = \sqrt{(x - R_{ij})^2 + y^2}$ , the electrostatic potential follows from Eq. (S13) as

$$\Psi_{\beta}(z_j, R_{ij}; x, y, z) = \frac{q_j}{2\pi\varepsilon_0} \int_0^{\infty} dK J_0(KR_{\parallel}) \frac{e^{-Kz_j}}{\varepsilon_{\alpha} K + \varepsilon_{\beta} \sqrt{K^2 + k_{\text{TF}}^2}} e^{\sqrt{K^2 + k_{\text{TF}}^2} z}. \quad (\text{S28})$$

Performing the volume integral in Eq. (S26) is a daunting task. We thus employ a numerical integration in  $\mathbf{r}$ . Figure S3(a) shows the potential  $\Psi_{\beta}$  for a point charge  $q_i = 1 \text{ e}$  located at a distance  $z_i = 1 \text{ nm}$  from a Thomas–Fermi metal characterized by a screening length  $\lambda = 1 \text{ nm}$ . As expected, one observes that the potential and the corresponding induced charge density in Fig. S3(b) extend over a characteristic length  $\sim 1 \text{ nm}$ . Contrary, for  $\lambda = 0.05 \text{ nm}$ , the potential is screened on  $\sim 0.05 \text{ nm}$  in Fig. S3(c) and the induced charge density in Fig. S3(d) approaches a point-like distribution as expected for a good metal.

Having assessed the numerical solution of Eqs. (S27) and (S28), we obtain the electrostatic energy by calculating the product  $u_{\lambda}^{\text{II}} = \rho^{\text{I}}(\mathbf{r}_i; \mathbf{r}) \Psi_{\beta}(\mathbf{r}_j; \mathbf{r})$  in Eq. (S26) on a mesh as shown in Fig. S4. Due to the approximately exponential decay, we employ a mesh of logarithmically increasing spacing with increasing distance to the position of the induced charges as indicated by the red lines in Fig. S4. We limit the integration to a distance from the charges of  $10\lambda$  in the lateral direction and  $8\lambda$  in the direction normal to the surface. The total image–image energy  $U_{\lambda}^{\text{II}} = \int d\mathbf{r} u_{\lambda}^{\text{II}}$  is then obtained by numerical integration using the corresponding volume element of each grid element. We explicitly checked that increasing the domain size does not alter the obtained energy as  $u_{\lambda}^{\text{II}} \sim 0$  at the boundary of the integration volume. Furthermore, due to the logarithmic grid employed, the integral converges well with the grid resolution as shown in Fig. S5. We characterize the meshing by a parameter  $m$ , which corresponds to the number of elements employed in the  $z$ -direction.

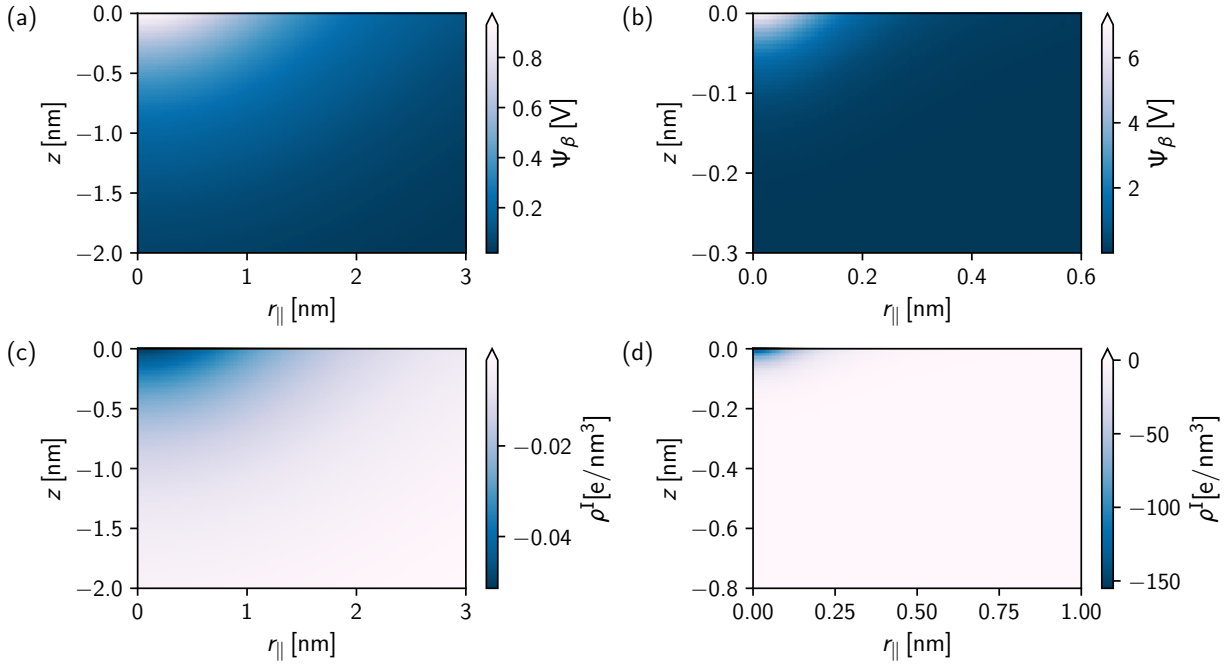


Figure S3. Electrostatic potential  $\Psi_\beta$  and charge density  $\rho^I$  induced by a point charge  $q_i = 1\text{e}$  in front of a TF interface. (a) Electrostatic potential in the  $y = 0$  plane for  $z_i = 1\text{ nm}$  and  $\lambda = 1\text{ nm}$ . (c) shows the corresponding induced charge density  $\rho^I$ . (b) and (d) show corresponding results for  $z_i = 0.1\text{ nm}$  and  $\lambda = 0.05\text{ nm}$ .

Figure S5 reports the convergence of  $\Delta U_m^{\text{II}} = U_m^{\text{II}}/U_{m=50}^{\text{II}}$ , where we consider  $m = 50$  as a reference. In practice, we find that  $m = 30$ , corresponding to a number of grid elements  $N_{\text{grid}} \sim 10^5$ , yields accurate results.

## II. THOMAS–FERMI ENERGY FOR A TWO-DIMENSIONAL IONIC CRYSTAL

Let us consider the total energy of a charge  $i$  interacting with all other charges  $j$  in the system,  $U_\lambda^i = \sum_{i \neq j} U_\lambda^{ij}$ . Taking the average over  $N$  particles,  $U_\lambda = \langle U_\lambda^i \rangle_N$ , we obtain the total electrostatic energy divided by the number of particles. For a two-dimensional square ionic crystal, the energy only depends on the distance  $d$  from the TF substrate and the crystal lattice spacing  $a_0$ . The expression corresponding to Eq. (S20) is thus given by

$$U_\lambda = U^{\text{CC}}(a_0) + U^{\text{CI}^\bullet}(d) + U_\lambda^{\text{CI}^\circ}(d, a_0) + U_\lambda^{\text{II}}(d, a_0). \quad (\text{S29})$$

The direct Coulomb interaction, which is independent of the TF substrate, only depends on the crystal lattice spacing  $a_0$ .  $U^{\text{CC}}(a_0)$  is thus conveniently expressed in terms of a Madelung constant

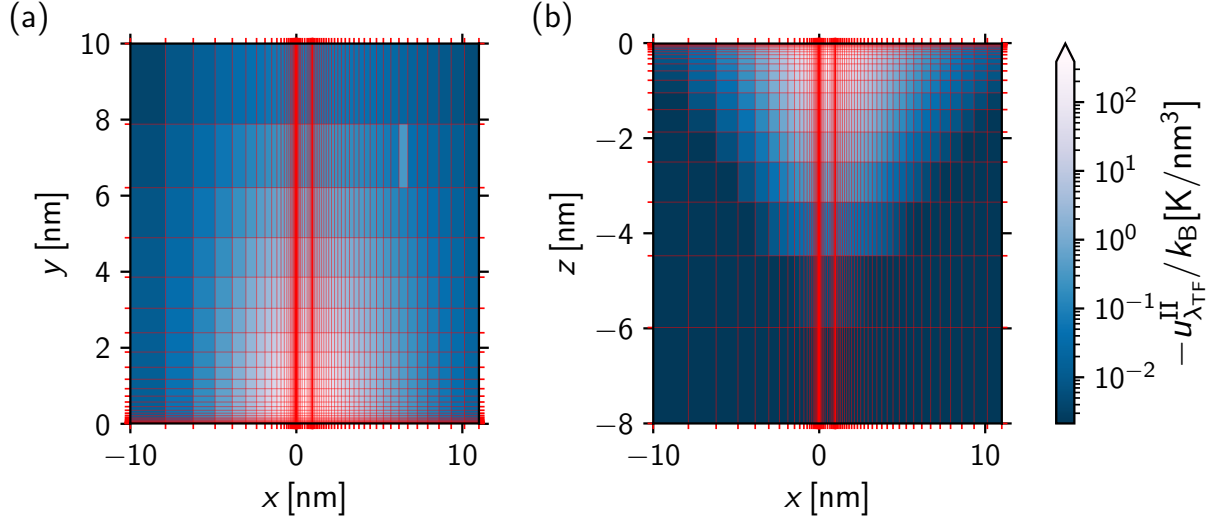


Figure S4. Energy density of the image–image interaction  $u_{\lambda}^{\text{II}}$  inside the TF substrate. The point charges  $q_i = -q_j = 1 \text{ e}$  are located at  $\mathbf{r}_i = (0, 0, 1 \text{ nm})$  and  $\mathbf{r}_j = (1 \text{ nm}, 0, 1 \text{ nm})$ , respectively. The TF substrate is characterized by a screening length  $\lambda = 1 \text{ nm}$ . Results are shown for (a) the  $z=0$  plane and (b) the  $y = 0$  plane. Red lines indicate the logarithmic mesh employed.

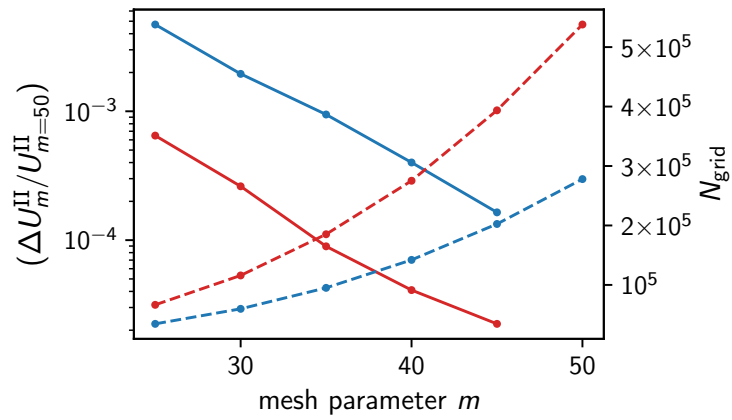


Figure S5. Convergence of the numerical integration of the image–image interaction energy with the resolution of the spatial grid (see Fig. S4). The mesh parameter  $m$  corresponds to the number of elements in the  $z$ -direction. The corresponding total number of elements  $N_{\text{grid}}$  is shown as dashed lines (right axis). For illustration, data are shown for two point charges at  $z_i = z_j = 1 \text{ nm}$ ,  $R_{ij} = 2 \text{ nm}$  using  $\lambda = 1 \text{ nm}$  (blue lines) and  $z_i = z_j = 0.1 \text{ nm}$ ,  $R_{ij} = 2 \text{ nm}$ ,  $R_{ij} = 2 \text{ nm}$  using  $\lambda = 0.05 \text{ nm}$  (red lines).

as discussed in Section **ID**. The one-body contribution  $U^{\text{CI}^\bullet}(d)$ , which only depends on  $d$ , is discussed in Section **IC**. Contrary,  $U_\lambda^{\text{CI}^\circ}$  and  $U_\lambda^{\text{II}}$  explicitly depend on the electrostatic screening characterized by  $\lambda$  and, thus, cannot be expressed in terms of a general Madelung constant. We explicitly perform the sum over all neighbors in the  $x, y$ -plane,

$$U_\lambda^{\text{CI}^\circ/\text{II}}(d, a_0) = \sum_{\substack{j, k = -\infty \\ k \neq j}}^{\infty} U_\lambda^{\text{CI}^\circ/\text{II}} \left( z_i = d, z_2 = d, R_{ij} = a_0 \sqrt{j^2 + k^2} \right) \Big|_{q_j = (-1)^{j+k}}. \quad (\text{S30})$$

In practice, we cut the infinite sum in Eq. (S30) at a finite number of neighbors  $N_{\text{neigh}}$ . We find that  $N_{\text{neigh}} \sim 10$  yields reasonable accuracy which we monitor by fitting the energy of the form  $U(N_{\text{neigh}}) = U(\infty) + U^\circ/N_{\text{neigh}}$ . Figure S6 shows  $U_\lambda^{\text{CI}^\circ}(N_{\text{neigh}})$  for  $\lambda = 1.1 \text{ nm}$ ,  $d = 0.8 \text{ nm}$  and  $a_0 = 1.475 \text{ nm}$  as employed in Fig. 3 of the main text. We perform a bootstrapping analysis discarding one data point each time during the fit to obtain the family of fitting parameters shown as lines in Fig. S6(a) and from which we obtain confidence intervals for  $N_{\text{neigh}} \rightarrow \infty$ . To obtain

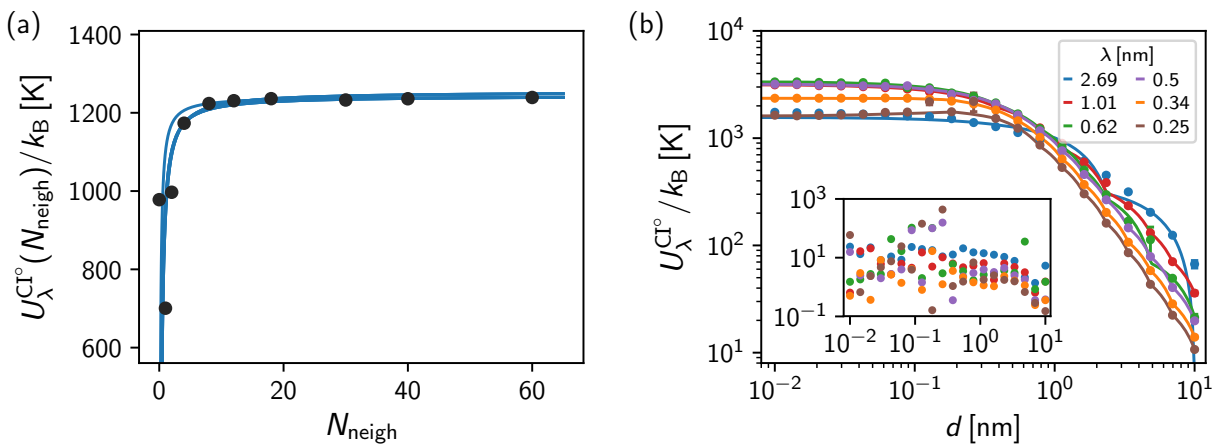


Figure S6. (a) Extrapolation of the neighbor sum for  $U_\lambda^{\text{CI}^\circ}$  as defined by Eq. (S30). Fits of the form  $U(\infty) + U^\circ/N_{\text{neigh}}$  are performed leaving out one data point each and shown as lines. (b) The resulting values  $U_\lambda^{\text{CI}^\circ}(N \rightarrow \infty)$  at varying distance for given  $\lambda$  are interpolated using a weighted smoothing spline. The inset shows the estimated numerical error from the fits in (a) which, in practice, is negligible. The same procedure is employed to obtain  $U_\lambda^{\text{II}}$ .

For  $U_\lambda^{\text{CI}^\circ/\text{II}}(d, a_0)$ , we interpolate the values obtained at a set of distances  $d$  using a weighted smoothing spline as shown in Fig. S6(b). The extrapolated numerical error estimate shown in the inset of Fig. S6(b) is, in all cases, negligible compared to the total charge-induced energy  $U^{\text{CI}}$  shown in Fig. 3(a) of the main text.

Table S1. Simulation parameters for the BMH potential employed for the salt–salt interaction<sup>a</sup>.

	$A$ [kcal/mol]	$\sigma$ [\AA]	$B$ [\AA]	$C$ [kcal/mol/\AA <sup>6</sup> ]	$D$ [kcal/mol/\AA <sup>8</sup> ]
Na–Na	6.0811	2.340	0.317	24.1807	11.5146
Cl–Cl	3.6487	3.170	0.317	1669.6786	3353.6227
Na–Cl	4.8639	2.755	0.317	161.2044	200.0662

<sup>a</sup> Parameters taken from Ref. [18].

### III. SIMULATION DETAILS

All our simulations are carried out using the LAMMPS simulation package [17] (stable release 7 Aug 2019) with periodic boundary conditions (PBC) in all dimensions. Electrostatic interactions are calculated using the PPPM method with an accuracy of at least  $10^{-5}$  and a real-space cut-off  $r_c = 12.5$  \AA. The non-electrostatic interactions are cut and shifted to zero at  $r_c$ . The non-electrostatic part of the salt–salt interactions are described using the Born-Meyer-Huggins potential,

$$U_{\text{BMH}}(r) = A \exp\left(\frac{\sigma - r}{B}\right) - \frac{C}{r^6} - \frac{D}{r^8}, \quad (\text{S31})$$

with parameters given in Table S1.

For the TF–TF interaction, we chose to employ a purely repulsive power law of the form  $U(r) = E/r^n$  to avoid numerical infinities when particles overlap. For our results shown in the main text, we use  $n = 8$  and  $E = 10^3$  kcal/mol/\AA<sup>8</sup>. The positive and negative TF particles differ only in their partial charge  $\pm q_{\text{TF}}$  and only interact electrostatically with the salt. To prevent mixing of the Thomas–Fermi fluid and the salt, a reflective wall of thickness  $e = 0.2$  nm is positioned between the two subsystems. The latter implies that, if an atom moves through the wall in a timestep by a distance  $\delta$ , its position is set back to  $-\delta$  away from the wall and the sign of the corresponding component of its velocity is flipped.

For the simulations of the TF and the salt in contact with an insulating/vacuum interface, the interactions between periodic images are not screened and we thus employ the slab correction by Yeh and Berkowitz [19] with a vacuum layer of three times the simulation cell height. Time integration is performed using a Verlet scheme with a timestep of 0.1 fs to allow for fast relaxation of the TF liquid of mass 0.1 amu. The mass of the Na and Cl atoms is set to 22.9898 and 35.446 amu, respectively. Temperature coupling for the TF at 12000 K and the salt at 2000 K is performed using separate Nose–Hoover thermostats with a characteristic time of 100 timesteps.

#### IV. INFLUENCE OF INTERACTION POTENTIALS, SALT SLAB WIDTH AND THOMAS–FERMI LAYER WIDTH

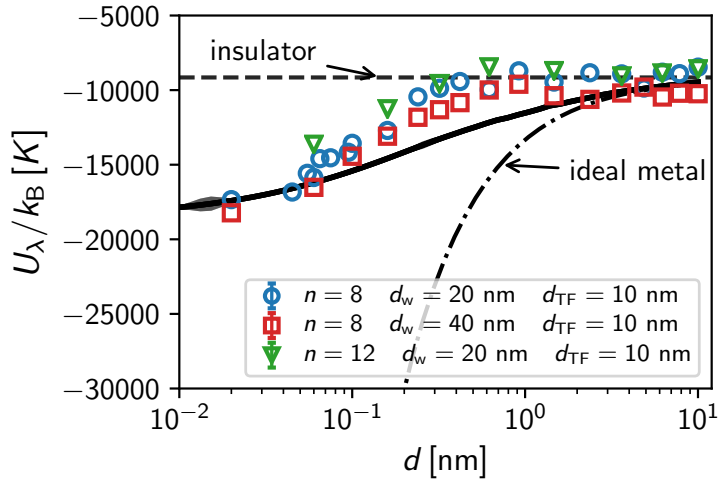


Figure S7. Influence of the TF–TF interaction potential (via the power  $n$ ) and wall–wall separation  $d_w$  on the resulting energy  $U_\lambda$ . All values are shown for  $\lambda^* = 0.5$  nm (see main text). The solid line denotes the numerical solution of the TF model.

To justify our choice of parameters  $n = 8$ ,  $d_w = 10$  nm and  $d_{TF} = 20$  nm, we here fix  $\lambda^* = 0.5$  nm and explicitly vary these parameters. Figure S7 shows the data from Fig. 3 in the main text (blue circles) together with the numerical solution of the TF model (solid black line). When varying the repulsive power law exponent to  $n = 12$ , the resulting energies (green triangles in Fig. S7) are in perfect agreement with  $n = 8$ . Upon increasing the distance between the two Thomas–Fermi interfaces to  $d_w = 40$  nm (red squares), the energies close to the surface (small  $d$ ) agree well. However, for  $d \gtrsim 0.2$  nm the energy is slightly smaller and in better agreement with the TF model prediction for a single interface (shown as solid black line in Fig. S7), hinting to possible interactions with the second interface.

In Fig. S8 we assess robustness of our results with respect to the influence of different TF layer thickness  $d_{TF}$ . Similar to  $d_w$ , an increase of  $d_{TF}$  enhances the agreement of  $U_\lambda$  with the TF model in Fig. S8(a). For our analysis provided in the main text,  $d_{TF} = 10$  nm was used (shown as red squares in Fig. S8(a)). The energy of the TF fluid  $U_\lambda^{\text{TF}}$  converges exponentially with  $d_{TF}$  with a decay length of about 5 nm, see Fig. S8 (b), where we show  $\Delta u_\lambda^{\text{TF}} = u_\lambda^{\text{TF}}(d_{TF}) - u_\lambda^{\text{TF}}(\infty)$  normalized by the extrapolated value at infinite layer thickness  $d_{TF}$ . To conclude, increasing  $d_w$  and  $d_{TF}$  slightly increases the agreement with the TF model of a single interface at the cost of significantly increased

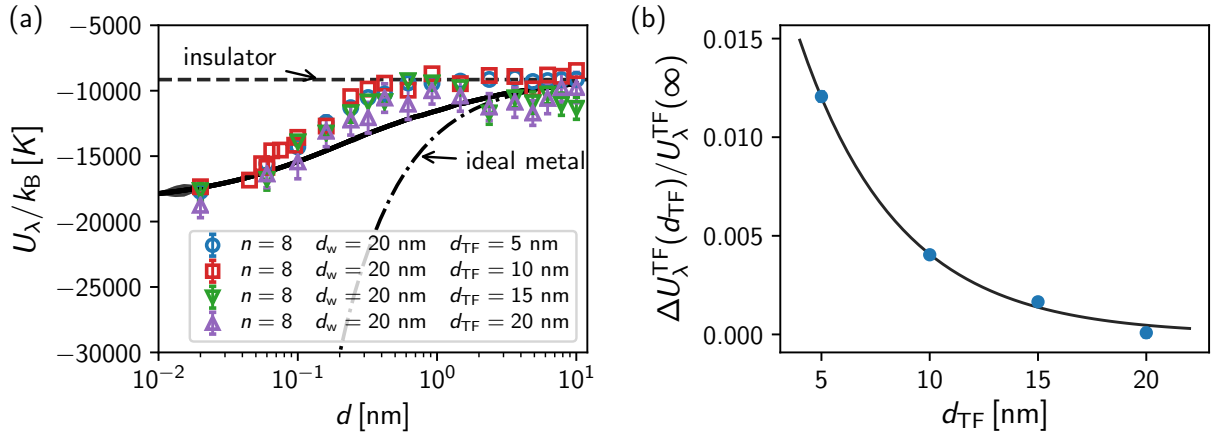


Figure S8. (a) Influence of  $d_{\text{TF}}$  on the electrostatic energy  $U_\lambda$  at fixed effective Thomas–Fermi length  $\lambda^* = 0.5 \text{ nm}$  (see main text).  $n = 8$  and  $d_w = 20 \text{ nm}$  correspond to the values used for Fig. 3 of the main text, where  $d_{\text{TF}} = 10 \text{ nm}$  was used. The solid line denotes the numerical solution of the TF model as discussed in the main text. (b) The disjoining energy of the Thomas–Fermi fluid decays exponentially with a decay length of  $\sim 5 \text{ nm}$  (solid line).

simulation effort (due to both an increase of the number of particles [ $\sim d_{\text{TF}}$ ] and the number of grid points necessary for the same accuracy using the PPPM method [ $\sim d_{\text{TF}} + d_w$ ]). Contrary, it is important to note that our simulation approach can deal with a finite thickness of the metallic substrate  $d_{\text{TF}}$ .

## V. ENERGY DECOMPOSITION FROM SIMULATION RERUNS

As discussed in the main text, the simulated electrostatic energy  $\tilde{U}_\lambda(d)$  consists of all ion pair contributions in Eq. (S20) and a contribution  $U_\lambda^{\text{TF}}$  corresponding to the self Thomas–Fermi fluid energy in the absence of the confined system. The total electrostatic energy between two charges  $i$  and  $j$  as measured in the molecular simulations thus reads:

$$\tilde{U}_\lambda(r_{ij}) = \tilde{U}^{\text{CC}}(z_i, z_j, R_{ij}) + \tilde{U}_\lambda^{\text{CI}}(z_i, z_j, R_{ij}) + \tilde{U}_\lambda^{\text{II}}(z_i, z_j, R_{ij}) + \tilde{U}_\lambda^{\text{TF}}(d_{\text{TF}}). \quad (\text{S32})$$

The latter contribution  $\tilde{U}_\lambda^{\text{TF}}$  can be seen as the ground-level energy of the Thomas–Fermi fluid in the simulation; the interaction between induced charges  $\tilde{U}_\lambda^{\text{II}}$  correspond accordingly to the change in its energy with respect to this reference. To compare the simulation/theoretical energies,  $\tilde{U}_\lambda^{\text{TF}}$  must be removed from  $\tilde{U}_\lambda(d)$  obtained in the simulation (since  $\tilde{U}_\lambda^{\text{TF}}$  is set to zero by definition in the Thomas–Fermi theory). The individual terms can be accessed from reruns of the simulation

trajectory. In detail, using configurations obtained for  $q = 1$  and  $q_{\text{TF}} \neq 0$ , we re-evaluate the electrostatic energy with either the salt charge  $q$  or the charge of the TF fluid  $q_{\text{TF}}$  set to zero. To compensate for the absence of screening between the periodic images, two-dimensional boundary conditions [19] are employed. The resulting energies read as

$$\tilde{U}_{\lambda}(r_{ij}) \Big|_{q_{\text{TF}}=0} = \tilde{U}^{\text{CC}}(z_i, z_j, R_{ij}) \quad \text{and} \quad (\text{S33})$$

$$\tilde{U}_{\lambda}(r_{ij}) \Big|_{q=0} = \tilde{U}_{\lambda}^{\text{II}}(z_i, z_j, R_{ij}) + \tilde{U}_{\lambda}^{\text{TF}}(d_{\text{TF}}). \quad (\text{S34})$$

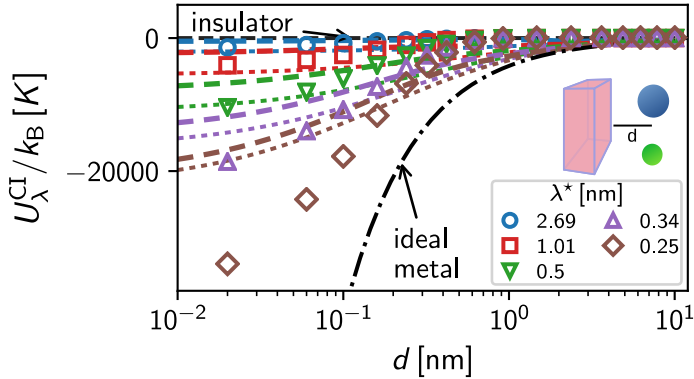


Figure S9. Energy  $U_{\lambda}^{\text{CI}}(d)$  between a 2D ionic crystal and a Thomas–Fermi metal separated by a distance  $d$  for different  $\lambda$ . For each  $\lambda$ , the symbols correspond to the effective simulation while the dashed line shows the Thomas–Fermi model (the dotted line is the one-body contribution  $U_{\lambda}^{\text{CI}^*}$  to  $U_{\lambda}^{\text{CI}}$ ). The black dash-dotted line shows the energy at a perfect metal surface  $U_{\lambda}^{\text{CI}}(d) = U_{\lambda}^{\text{CI}^*}(d) \sim 1/d$ . The black dashed line  $U_{\lambda}^{\text{CI}}(d) = 0$  corresponds to data for an insulating surface.

Subtracting Eqs. (S33) and (S34) from Eq. (S32) yields the contribution  $\tilde{U}_{\lambda}^{\text{CI}}$

$$\tilde{U}_{\lambda}(r_{ij}) - \tilde{U}_{\lambda}(r_{ij}) \Big|_{q_{\text{TF}}=0} - \tilde{U}_{\lambda}(r_{ij}) \Big|_{q=0} = \tilde{U}_{\lambda}^{\text{CI}}(z_i, z_j, R_{ij}). \quad (\text{S35})$$

Fig. S9 shows  $U_{\lambda}^{\text{CI}}$  as a function of  $d$  for different  $\lambda$ .  $U_{\lambda}^{\text{CI}}$  decays with  $d$  and, more importantly, varies between the values for an insulator [ $U_{\lambda}^{\text{CI}}(d) = 0 \forall d$ ] and a perfect metal [ $U_{\lambda}^{\text{CI}}(d) = U_{\lambda}^{\text{CI}^*}(d) = e^2/(16\pi\epsilon_0\epsilon_0 d)$ , i.e. the charge image model].

To decompose  $\tilde{U}_{\lambda}^{\text{II}}$  and  $\tilde{U}_{\lambda}^{\text{TF}}$ , we perform a separate set of simulations with the TF fluid confined between two reflecting walls and using the slab correction of Ref. [19] to mimic an insulating vacuum.

In Figure S10, we show  $U^{\text{II}}$  obtained from Eq. (S25) and using the extrapolation of the neighbor sum described in Section II. In general,  $U^{\text{II}}$  is small compared to  $U^{\text{CI}}$  shown in Fig. 3(a) of the main text. Upon decreasing  $\lambda$  (better metal), the induced charge density is more localized and the

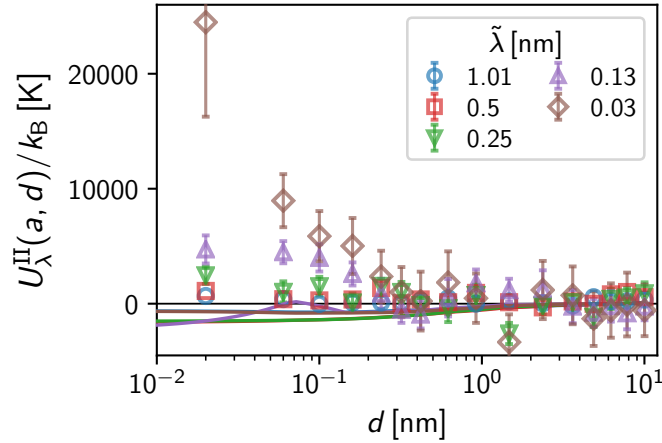


Figure S10. Electrostatic energy due to the induced charge densities,  $U_{\lambda}^{\text{II}}$ , for the systems discussed in Fig. 2 of the main text. Data points show the simulated values obtained according to Eq. (S34), lines show the results from numerical integration of Eq. (S25) and extrapolating the neighbor sum as described in Section II.

potential gets screened on shorter distances. Consequently, this term decays to zero in the perfect metal limit. As discussed in the main text, our simulations (data in Fig. S10) show the opposite behavior due to the imperfect nature of the TF fluid. The configuration of lowest energy for a system of point charges is the homogeneous distribution and localizing any charge distribution to form  $\rho^{\text{I}}$  necessarily increases this energy. This differs from the ideal electron gas behavior in the TF model, which has zero energy in the homogeneous case, where by inducing a charge density the resulting energy will become negative (lines in Fig. S10). Note that this deviation from ideality is captured in the rescaling of the effective screening  $\tilde{\lambda}$  introduced in the main text.

## VI. GENERAL CONNECTION TO SCREENING IN LINEAR DIELECTRIC MEDIA

To obtain an explicit expression for the screened potential  $\Psi_{\beta}$ , we follow the basic equations of classical theory of electric polarization [1]. We consider a perturbing charge distribution  $\rho^{\text{ext}}(\mathbf{r})$  located inside the metal, see Fig. S11. According to Poisson equation,  $\rho^{\text{ext}}$  creates a potential  $-\nabla^2 \Psi^{\text{ext}}(\mathbf{r}) = \rho^{\text{ext}}(\mathbf{r})/\varepsilon_0 \varepsilon_{\beta}$ , which in turn induces a charge density  $\rho^{\text{I}}$ . Denoting the full charge density  $\rho(\mathbf{r}) = \rho^{\text{ext}}(\mathbf{r}) + \rho^{\text{I}}(\mathbf{r})$ , the full physical potential is  $-\nabla^2 \Psi(\mathbf{r}) = \rho(\mathbf{r})/\varepsilon_0 \varepsilon_{\beta}$ . In analogy to linear dielectric media, a linear relation between  $\Psi$  and  $\Psi^{\text{ext}}$  yields

$$\Psi^{\text{ext}}(\mathbf{r}) = \int d\mathbf{r}' \varepsilon(\mathbf{r}, \mathbf{r}') \Psi(\mathbf{r}'), \quad (\text{S36})$$

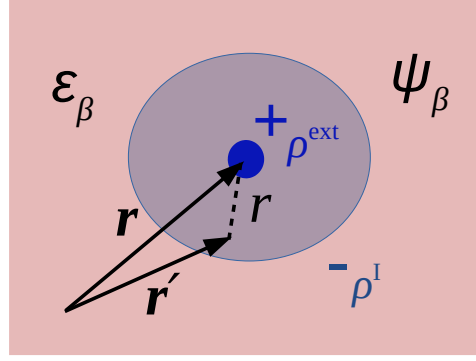


Figure S11. Illustration of a perturbing charge distribution  $\rho^{\text{ext}}$  and the induced charge density  $\rho^{\text{I}}$  inside the metal  $\beta$ , respectively.

where we have introduced the non-local dielectric response function  $\varepsilon(\mathbf{r}, \mathbf{r}')$ . For a spatially uniform electron gas translational invariance can be used, i.e.  $\varepsilon(\mathbf{r}, \mathbf{r}') = \varepsilon(|\mathbf{r} - \mathbf{r}'|)$ . Equation (S36) can be solved for  $\Psi_\beta$  using Fourier transform and the convolution theorem [20]

$$\Psi(\mathbf{k}) = \frac{1}{\varepsilon(\mathbf{k})} \Psi^{\text{ext}}(\mathbf{k}). \quad (\text{S37})$$

Equation (S37) shows that, for each wavevector  $\mathbf{k}$ , the total electrostatic potential  $\Psi$  is given by the external potential  $\Psi^{\text{ext}}$  at the same  $\mathbf{k}$  but screened by a factor  $1/\varepsilon(\mathbf{k})$ , the Thomas–Fermi dielectric constant [6].

We now use a linear relation between the (Fourier transformed) induced charge density and the electrostatic potential,  $\rho^{\text{I}}(\mathbf{k}) = -\chi(\mathbf{k})\Psi(\mathbf{k})$ , where  $\chi(\mathbf{k})$  is the dielectric susceptibility and  $\varepsilon(\mathbf{k}) = (1 + \chi(\mathbf{k}))\varepsilon_0$ . Comparison with Eq. (S3) yields the TF dielectric susceptibility [6],

$$\chi_{\text{TF}}(\mathbf{k}) = e^2 \frac{\partial n_0}{\partial \mu}. \quad (\text{S38})$$

Thus, it is convenient to define the TF wavevector as given in Eq. (S4)

$$k_{\text{TF}}^2 = \frac{e^2}{\varepsilon_0} \frac{\partial n_0}{\partial \mu}, \quad (\text{S39})$$

from which the Thomas–Fermi dielectric constant follows as

$$\varepsilon(\mathbf{k}) = 1 + \frac{k_{\text{TF}}^2}{k^2}. \quad (\text{S40})$$

To shed light on the significance of  $\lambda$ , we now consider the case of a point charge  $\rho^{\text{ext}}(\mathbf{r}) = q\delta(\mathbf{r} - \mathbf{r}')$  as defined in Fig. S1(b). Using  $\mathbf{r} - \mathbf{r}' = \mathbf{r}$ , the external potential of the point charge and its Fourier transform directly follow from Poisson equation as

$$\Psi^{\text{ext}}(r) = \frac{q}{4\pi\varepsilon_0 r} \quad \text{and} \quad \Psi^{\text{ext}}(k) = \frac{q}{\varepsilon_0 k^2}. \quad (\text{S41})$$

Using Eqs. (S37) and (S40), the total potential in the metal is given by

$$\Psi(k) = \frac{1}{\varepsilon(k)} \Psi^{\text{ext}}(k) = \frac{q}{\varepsilon_0 (k^2 + k_{\text{TF}}^2)}, \quad (\text{S42})$$

which, upon inverse Fourier transformation, yields

$$\Psi(r) = \int \frac{dk}{(2\pi)^3} e^{ikr} \frac{q}{\varepsilon_0 (k^2 + k_{\text{TF}}^2)} = \frac{q}{4\pi\varepsilon_0 r} e^{-k_{\text{TF}}r}. \quad (\text{S43})$$

Equation (S43) has the form of a screened Coulomb potential and  $\lambda = k_{\text{TF}}^{-1}$  is analogous to the Debye screening length  $\lambda_D$  obtained for electrolyte solutions [21]. This analogy forms the motivation for the explicit TF fluid screening approach in the present work.

- [1] J. D. Jackson, *Classical Electrodynamics* (Wiley, New York, 1999).
- [2] N. D. Lang and W. Kohn, *Phys. Rev. B* **7**, 3541 (1973).
- [3] L. H. Thomas, *Math. Proc. Camb. Philos. Soc.* **23**, 542 (1927).
- [4] E. Fermi, *Rend Accad Naz Lincei* **6**, 32 (1927).
- [5] R. Baer, “Electron density functional theory,” (2016).
- [6] N. W. Ashcroft and N. D. Mermin, *Solid State Physics* (Holt, Rinehart and Winston, 1976).
- [7] The electrons obey the Fermi–Dirac distribution function,

$$n_0(\mu) = \mathcal{D}(\mu) \times \frac{1}{\exp\left(\frac{\mu - \mathcal{E}_F}{k_B T} + 1\right)},$$

such that in the limit  $\mathcal{E}_F/k_B T \rightarrow \infty$  the second term results in a Heaviside step function,  $n_0(\mu) = \mathcal{D}(\mu)\Theta(\mu - \mathcal{E}_F)$ . Taking the derivative  $\partial n_0/\partial\mu = \mathcal{D}(\mu)\delta(\mu - \mathcal{E}_F) = \mathcal{D}(\mathcal{E}_F)$  yields the density of states valid for  $T \ll T_F$ .

- [8] V. Kaiser, J. Comtet, A. Niguès, A. Siria, B. Coasne, and L. Bocquet, *Faraday Discuss.* **199**, 129 (2017).
- [9] I. Bronshtein, K. Semendyayev, G. Musiol, and H. Mühlig, *Handbook of Mathematics : With 132 Tables*, 6th ed. (Springer, 2015).
- [10] D. M. Newns, *J. Chem. Phys.* **50**, 4572 (1969).
- [11] J. C. Inkson, *J. Phys. C: Solid State Phys.* **6**, 1350 (1973).
- [12] A. A. Kornyshev, A. I. Rubinshtein, and M. A. Vorotyntsev, *Phys. Status Solidi B* **84**, 125 (1977).
- [13] R. R. Netz, *Phys. Rev. E* **60**, 3174 (1999).
- [14] M. M. Taddei, T. N. C. Mendes, and C. Farina, *Eur. J. Phys.* **30**, 965 (2009).
- [15] J. Lekner, *Physica A: Statistical Mechanics and its Applications* **176**, 485 (1991).
- [16] S. Tyagi, *Prog Theor Phys* **114**, 517 (2005).
- [17] S. Plimpton, *J. Comput. Phys.* **117**, 1 (1995).

[18] J. Anwar, D. Frenkel, and M. G. Noro, *J. Chem. Phys.* **118**, 728 (2002).

[19] I.-C. Yeh and M. L. Berkowitz, *J. Chem. Phys.* **111**, 3155 (1999).

[20] Using the following definition of the Fourier transform of a function  $f$ :

$$f(\mathbf{k}) = \int d\mathbf{r} e^{-i\mathbf{kr}} f(\mathbf{r}) \quad \text{and} \quad f(\mathbf{r}) = \frac{d\mathbf{k}}{(2\pi)^3} e^{i\mathbf{kr}} f(\mathbf{k})$$

[21] P. Debye and E. Hückel, *Phys Zft* **24**, 305 (1923).